JOURNAL OF GEOPHYSICAL RESEARCH, VOL. 115, C12049, doi:10.1029/2010JC006331, 2010

A nonhydrostatic version of FVCOM: 2. Mechanistic study of tidally generated nonlinear internal waves in Massachusetts Bay

Zhigang Lai,[1] Changsheng Chen,[1,2] Geoffrey W. Cowles,[1] and Robert C. Beardsley[3]

Received 9 April 2010; revised 11 October 2010; accepted 15 October 2010; published 21 December 2010.

[1] The generation, propagation, and dissipation processes of large-amplitude nonlinear internal waves in Massachusetts Bay during the stratified season were examined using the nonhydrostatic Finite-Volume Coastal Ocean Model (FVCOM-NH). The model reproduced well the characteristics of the high-frequency internal waves observed in Massachusetts Bay in August 1998. The model experiments suggested that internal waves over Stellwagen Bank are generated by the interaction of tidal currents with steep bottom topography through a process of forming a large-density front on the western slope of the bank by the release of an initial density perturbation near ebb-flood transition, nonlinear steepening of the density front into a deep density depression, and disintegrating of the density depression into a wave train. Earth's rotation tends to transfer the cross-bank tidal kinetic energy into the along-bank direction and thus reduces the intensity of the density perturbation at ebb-flood transition and density depression in the flood period. The internal wave packet propagates as a leading edge feature of the internal tidal wave, and the faster propagation speed of the high-frequency internal waves in Massachusetts Bay is caused by Earth's rotation. The model experiments suggested that bottom friction can significantly influence the cross-bank scale of the density perturbation and thus the density depression during wave generation and the dissipation during the wave's shoaling. Inclusion of vertical mixing using the Mellor-Yamada level 2.5 turbulence closure model had only a marginal effect on wave evolution. The model results support the internal wave theory proposed by Lee and Beardsley (1974) but are in disagreement with the lee-wave mechanism proposed by Maxworthy (1979).

Citation: Lai, Z., C. Chen, G. W. Cowles, and R. C. Beardsley (2010), A nonhydrostatic version of FVCOM: 2. Mechanistic study of tidally generated nonlinear internal waves in Massachusetts Bay, *J. Geophys. Res.*, *115*, C12049, doi:10.1029/2010JC006331.

1. Introduction

[2] Stellwagen Bank is located on the eastern reaches of Massachusetts Bay. It is elliptical in plan view, with a major axis of 31 km in the north-south direction and a distance of ~20 km along the minor axis in the west-east direction (Figure 1). In the vertical, the shallow bank is a major underwater obstacle between Massachusetts Bay and Gulf of Maine. The cross-bank bottom topography rises gradually with a slope of 0.0032 (over a distance of 12.5 km) from 70 m on the eastern edge to 30 m on the western edge, and then falls off rapidly with a slope of ~0.04 to a depth of 90 m along the western slope. In late summer and early fall, during which time the water is highly stratified, energetic high-frequency internal waves are ubiquitous around Stellwagen Bank. These wave packets, generating visible banded surface slicks and propagating westward toward the Massachusetts coast, were first reported by *Halpern* [1971a, 1971b], extensively observed later by *Haury et al.* [1979] and *Chereskin* [1983], and more recently by *Butman et al.* [2006a, 2006b].

[3] Similar to the production of internal waves reported by *Gargett* [1976] in the Strait of Georgia, *Farmer and Smith* [1978] in Knight Inlet, and *Armi and Farmer* [1988] in the Strait of Gibraltar, the large-amplitude, high-frequency internal waves seen in Massachusetts Bay are generated through an interaction of the barotropic tide and topography. Temperature observations made by *Halpern* [1971a, 1971b] on a mooring located 9 km west of Stellwagen Bank showed that the internal wave train is observed on the incoming tidal flow and is first noticeable as an abrupt rise in the upper water column temperature followed by a group of high-

---

[1] School for Marine Science and Technology, University of Massachusetts Darmouth, New Bedford, Massachusetts, USA.

[2] Also at Marine Ecosystem and Environment Laboratory, College of Marine Science, Shanghai Ocean University, Shanghai, China.

[3] Department of Physical Oceanography, Woods Hole Oceanographic Institution, Woods Hole, Massachusetts, USA.

0148-0227/10/2010JC006331

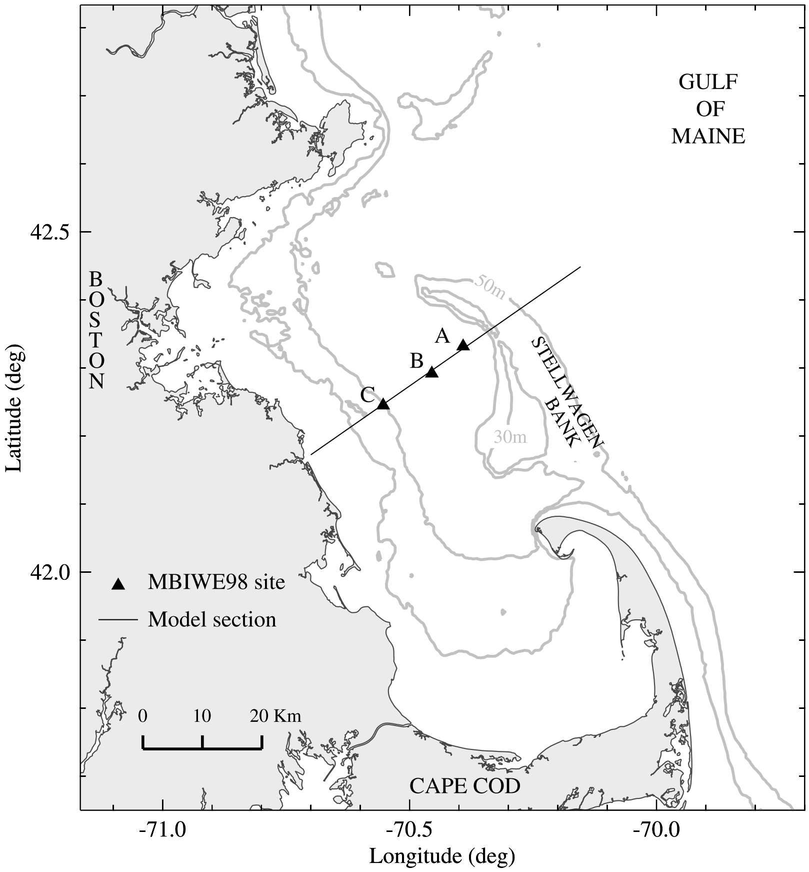

Figure 1. Schematic of Massachusetts Bay and Stellwagen Bank and transect used to construct the two-dimensional numerical model. Triangles are the MBIWE98 measurement sites A, B, and C.

frequency waves of depression. However, it was not clear in this and later field studies what processes caused the initial wave generation before the well-defined packets were observed in Stellwagen Basin. *Haury et al.* [1979] observed the formation of a large lee wave that formed over the eastern slope of Stellwagen Bank on the ebb (eastward) and hypothesized that this lee wave led to the wave packets observed west of the bank on the flood tide. *Chereskin* [1983] determined the time development of this ebb tide lee wave using acoustic measurements and showed its relationship to supercritical flow conditions on the bank. However, her data failed to show that this lee wave could propagate across the bank during the ebb-flood tidal transition and enter the interior of Massachusetts Bay. In August 1998, a comprehensive field experiment for internal waves (hereby referred as MBIWE98) was conducted in Massachusetts Bay by *Butman et al.* [2006a, 2006b]. Their observations revealed that the formation of the high-frequency internal waves on the western side of the bank is a result of a deep depression of isotherms that appears shortly after the flooding tide. The wave packets then propagate toward the coast at an average speed of 60 cm/s.

[4] There are many theoretical and laboratory studies of internal waves that elucidate ocean observations [see, e.g., *Vlasenko et al.*, 2005; *Helfrich and Melville*, 2006; *Scotti et al.*, 2007]. In particular, the earlier work of *Lee and Beardsley* [1974] and *Maxworthy* [1979] provided two different mechanisms for the generation of the wave packets seen in Massachusetts Bay. Stimulated by *Halpern*'s [1971a] observation that the wave packet was characterized by a large abrupt rise in temperature and elevated temperature level in the wave packet over the background, *Lee and Beardsley* [1974] (hereafter referred to as LB) proposed that the generation of internal waves over Stellwagen Bank can be divided into three distinct phases: (1) the formation of an initial temperature front on the western side of the bank as a result of "partial blocking" [*Baines*, 1987] of the stratified tidal flow by topography; (2) nonlinear steepening of the temperature front; and (3) evolution into a wave train owing to the effects of dispersion and nonlinearity (Figure 2, left). *Maxworthy* [1979], however, found from laboratory experiments that the blocking effect of an obstacle on an oncoming tidal flow can only result in a quasi-stationary lee wave with a phase velocity opposite the flow direction. Such a lee wave cannot propagate against the flow in the upstream direction until its phase velocity exceeds the slackening tidal current. On this basis, he suggested that the westward propagating internal wave train observed in Massachusetts Bay originates from a single lee wave created during the previous ebb tide (Figure 2, right). The wave is able to propagate upstream only as the ebb tide slacks on the eastern side of Stellwagen Bank. It then undergoes nonlinear steepening as it traverses the bank and subsequently forms an internal wave train.

[5] It should be noted that the major differences between the explanations of LB and *Maxworthy* [1979] are tidal phase and location associated with wave generation. LB's

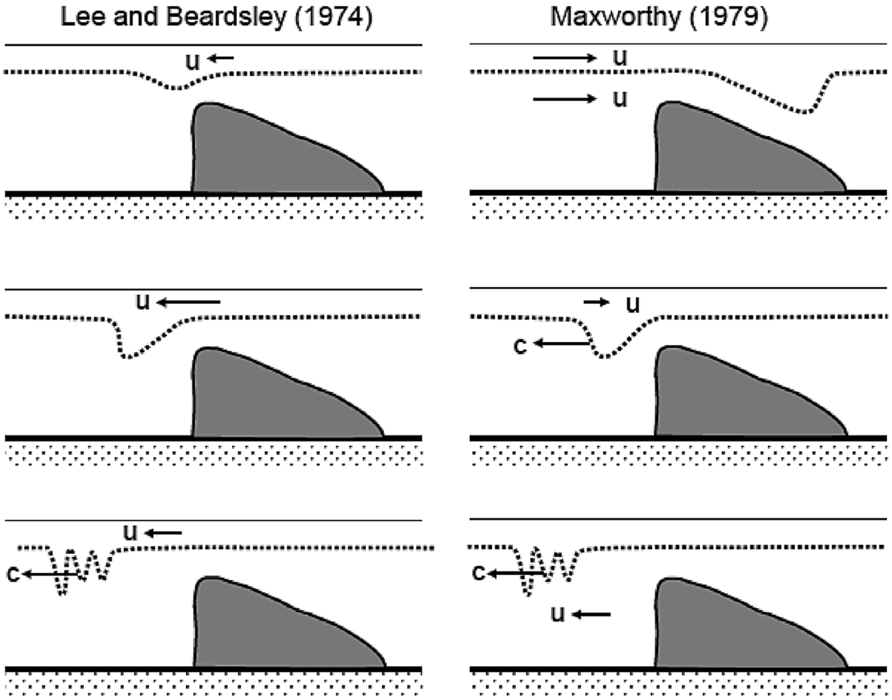

Figure 2. Schematics of the mechanisms for generation of internal waves proposed by *Lee and Beardsley* [1974] and *Maxworthy* [1979]. See section 1 for detailed explanations.

theory suggests that the temperature front is generated during flood tide on the western side of the bank. In contrast, Maxworthy's theory proposes that the temperature front results from the disintegration of a single lee wave created during the previous ebb tide, subsequently propagating over the topography as the tide current slackens. Some support for LB's theory can be found in the field studies of *Halpern* [1971a, 1971b] and *Butman et al.* [2006a, 2006b], who observed the internal wave packets on the western side of the bank during flood tide. Lee waves, as observed in Maxworthy's laboratory experiments, were evident on the eastern side of Stellwagen Bank in the field measurements of *Haury et al.* [1979] and *Chereskin* [1983]. These measurements, however, did not show either a westward propagation of the lee wave into the western side of the bank or any subsequent disintegration into the high-frequency wave packet during propagation upstream over the topography. Since the bottom slope on the eastern flank of Stellwagen Bank is only 1/10 that of the western slope, the intensity of the lee wave observed on the eastern side of the bank is relatively weak, with a width of ~7 km [*Haury et al.*, 1979]. In actuality, the transition from ebb to flood tide over Stellwagen Bank occurs rather rapidly and the internal depression, which has been observed over the eastern side of the bank during the ebb tide, shortens and shoals as the magnitude of the incoming flood tide increases [*Chereskin*, 1983]. The critical issue in the context of Maxworthy's theory is whether or not the lee wave is able to propagate across Stellwagen Bank during the ebb-flood transition. This question, however, has not been explored in detail.

[6] Compared to theoretical and laboratory studies, numerical simulation of internal waves provides another approach to investigate these time-dependent, nonlinear waves. Such an attempt in Massachusetts Bay was first made by LB to simulate the internal wave packets observed by *Halpern* [1971a] and later by *Hibiya* [1988] to study wave generation indicated from the acoustic data of *Chereskin* [1983]. Recently, *Scotti et al.* [2007, 2008] conducted a more comprehensive numerical experiment to study the entire process of internal wave generation, propagation and dissipation in Massachusetts Bay. Employing a two-dimensional nonrotating inviscid vorticity-stream function model, they demonstrated that the observed internal wave packets in Massachusetts Bay start as a density depression over the eastern slope of Stellwagen Bank during ebb tide. But they disputed the lee wave mechanism in that it is the relaxation of the density depression rather than the upstream propagation of the lee wave over the topography that generates the internal waves. Their studies also showed that the generation and propagation of internal waves are influenced by the intensity of tidal forcing and stratification. However, since the model was inviscid, they were not able to investigate the influence of turbulent mixing and bottom friction on the propagation and dissipation of the internal wave packets. Moreover, Stellwagen Bank is a shallow bank characterized by strong cross-bank tidal currents that are expected to generate a residual around-bank flow. The tidal rectification process, resulting from the nonlinear interaction of tidal currents over steep bottom topography [*Loder*, 1980; *Chen and Beardsley*, 1995; *Chen et al.*, 1995], transfers the tidal energy to the residual flow via bottom friction and Coriolis force as the tidal wave propagates cross the bank. This can potentially affect the intensity of the density depression and thus the generation of internal waves on the western side of the bank. However, this effect was not

resolved in the inviscid nonrotating model studies of *Scotti et al.* [2007, 2008].

[7] In this paper we investigate in detail the different mechanisms involved in producing the tidally generated nonlinear internal waves found in Massachusetts Bay. Specifically, we seek to understand how the initial density perturbation evolves before the well-defined internal wave packets are observed. Since nonlinear internal waves generated by interactions of tide and topography are common features in many coasts and estuaries, we feel that this study represents a more general case with potential value for similar studies in other regions. This work is achieved by using the recently developed the nonhydrostatic Finite-Volume Coastal Ocean Model (FVCOM-NH) [see *Lai et al.*, 2010]. In doing that, we first examine the capability of FVCOM-NH to simulate the internal waves observed in MBIWE98, and then explore the process of the formation of the density depression during the period of internal wave generation. A number of numerical experiments were made to explore the influence of critical parameters on the characteristics of wave generation and propagation. These include: (1) cases with varying tidal intensity, stratification, bottom friction, and vertical turbulent mixing to examine the respective influence of these variables and processes; (2) cases with and without Coriolis force to evaluate the impacts of the large-scale tidal-topographic interaction on the formation of small-scale internal waves; and (3) cases with idealized bathymetry to identify the possible role of the bank's slope and width on the generation and propagation of internal waves.

2. Model and Experiment Design

[8] This study is conducted using FVCOM-NH, a nonhydrostatic version of FVCOM; see *Lai et al.* [2010] for model description, discrete structure, solution methods, numerical algorithms, and validation experiments. FVCOM is the unstructured grid Finite-Volume Coastal Ocean Model originally developed by *Chen et al.* [2003] and continually updated through a team effort [*Chen et al.*, 2006a, 2006b, 2007; *Cowles*, 2008; *Huang et al.*, 2008]. The major modifications to the hydrostatic version of FVCOM are to include the vertical momentum equation and implement a Poisson equation to evolve the three-dimensional nonhydrostatic pressure field (e.g., a similar approach was applied by *Mahadevan et al.* [1996], *Marshall et al.* [1997], *Casulli* [1999], *Kanarska and Maderich* [2003], and *Fringer et al.* [2006]). By decomposing the pressure into hydrostatic and nonhydrostatic components, FVCOM-NH is coded with a flexible modular structure, which allows a user to activate or deactivate easily the nonhydrostatic solution procedure, depending on the problem of interest. FVCOM-NH is solved numerically with an option of split-mode explicit or semi-implicit time stepping method and is parallelized using MPI for execution on both distributed and shared memory systems. To improve model efficiency, the matrix constructed from the discrete pressure Poisson equation is solved using the high-performance scalable sparse matrix solver library PETSc [*Balay et al.*, 2007] and an efficient preconditioner package (HYPRE) [*Falgout and Yang*, 2002].

[9] FVCOM-NH has been well validated using a wide range of idealized oceanic problems. These include surface standing and solitary waves in idealized flat- and sloping-bottom channels in homogeneous conditions, the density adjustment problem for lock-exchange flow in a flat-bottom channel, and two-layer internal solitary wave breaking on a sloping shelf (see *Lai et al.* [2010] for detailed model-data comparisons). For example, the surface standing wave case is used to test the split mode explicit and semi-implicit time stepping method for nonhydrostatic primary equations; the lock-exchange case is used to check the mass conservation and examine the numerical dissipation properties of the discrete algorithms; the internal wave breaking on a linear slope case is used to assess the capability of FVCOM-NH to realistically represent the frequently observed energetic event in the coastal ocean. In summary, these validation efforts demonstrate that FVCOM-NH is able to resolve small-scale nonhydrostatic processes with excellent conservation of local and global mass with second-order numerical accuracy. This is a prerequisite for the success of applying the model to the simulation of large-amplitude, nonlinear internal waves in Massachusetts Bay. For the current work, the semi-implicit time stepping method was employed to allow a larger model time step by removing the constraint imposed by the surface gravity wave celerity.

[10] The internal waves observed over Stellwagen Bank propagate orthogonal to the isobaths [*Trask and Briscoe*, 1983]. For simplification, all previous theoretical and numerical modeling study of internal waves in this region used a two-dimensional model approach without consideration of the along-isobath variation in momentum and temperature or density equations [LB; *Hibiya*, 1988; *Scotti et al.*, 2007, 2008]. In order to compare with previous studies, we also used a two-dimensional approach in which (x, z) are defined as the cross-bank and vertical axes, respectively. The major difference from previous two-dimensional modeling is that in the present work we also include the influence of the Coriolis force, fully turbulent mixing, and bottom friction. This enables us to examine their respective roles in the internal wave generation and propagation through a suite of numerical experiments.

[11] The computational domain comprises a transect perpendicular to Stellwagen Bank, running from the eastern side of the bank to the Massachusetts coast (Figure 1). This is the same transect that was used in the modeling efforts of *Scotti et al.* [2007] and is the transect along which the MBIWE98 measurements (sites A, B and C) were made. A nonuniform horizontal grid resolution is used in the cross-bank direction, with a fine-scale grid of 15 m covering the entire region of wave generation, propagation and shoaling/dissipation, stretching to coarser resolution (200 m) near the open boundary and coastal region (Figure 3). In the vertical, 45 uniform sigma layers are used, which corresponds to a vertical resolution of ~2 m in the deepest region and ~0.7 m at the crest of the bank. This configuration provides sufficient resolution to resolve high-frequency internal waves while remaining within practical computational limits. The fine grid size used in this study was established using a grid convergence study in which the model was run with resolutions of 100 m, 50 m, 20 m, 15 m and 10 m under the same physical conditions. Comparisons were then made of the internal

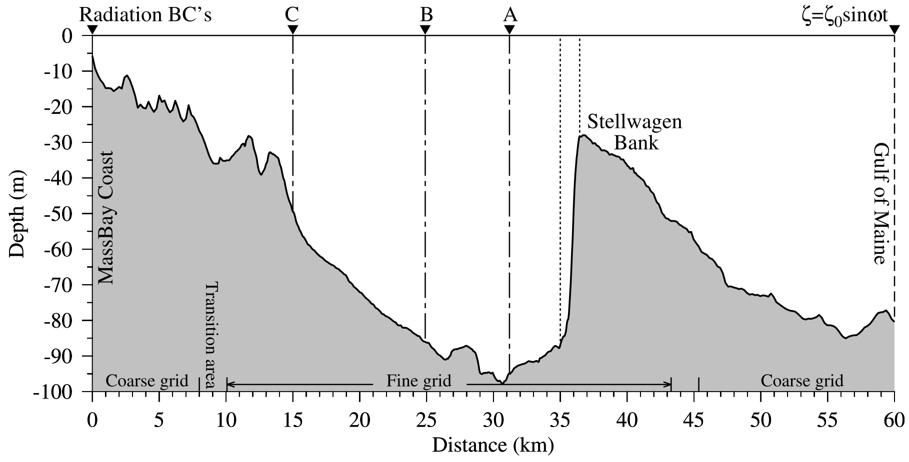

Figure 3. Bathymetry of FVCOM-NH model on the cross-bay transect shown in Figure 1. The model is driven by tidal forcing specified as $\zeta = \zeta_o \sin \omega t$ at the open boundary. Here ζ is the free surface elevation, and ζ_o and ω are the amplitude and frequency of the M_2 tide. The spring, mean, and neap tidal forcing are specified by adjusting ζ_o. A gravity wave radiation boundary condition is specified on the shore side boundary under the assumption that zero energy reflects back into the interior from the coast. The computational domain features a nonuniform horizontal grid (see section 2 for details). A, B, and C are the locations of the MBIWE98 measurement sites (also shown in Figure 1).

wavefield over time as represented by the pycnocline response. In summary, we found that the model-computed high-frequency internal waves are present only when the grid size was reduced to 20 m. With further refinement, the model-produced internal waves display slight differences but the broad features such as the amplitude of leading depression and the number of resolved individual waves remained the same. To optimize the computational load, we used a 15 m grid resolution in the current work. In a separate grid resolution study, *Scotti et al.* [2007] established a similar configuration.

[12] The model is forced by M_2 barotropic tidal forcing at the open boundary. The tidal amplitude used here is exported directly from a regional-scale FVCOM Gulf of Maine model (FVCOM-GOM) (C. Chen et al., Tidal dynamics in the Gulf of Maine and New England Shelf: An application of FVCOM, unpublished manuscript, 2006). Unlike *Scotti et al.* [2007], a gravity wave radiation condition is specified at the western (coastal) boundary to allow the tidal wave to propagate out of computational domain with minimum reflection. A sponge layer with a damping coefficient of 0.0005 is added along this boundary to absorb the internal wave energy. This specification is physically relevant as no existing observations have detected internal waves propagating eastward from the nearshore region owing to the strong dissipation of the westward traveling internal wave energy in the shallow region along the coast [*Scotti et al.*, 2007].

[13] The initial density profiles are generated following the equation in the work of *Scotti et al.* [2007], which represent well the observed August stratification in the Middle of Massachusetts Bay during MBIWE98. To exam-

Table 1. Tidal Amplitude at the Open Boundary and Model-Predicted Maximum Horizontal Velocity at the Crest and in Midbasin

Case	Forcing Amplitude (m)	Maximum Velocity at Crest (m/s)	Maximum Velocity in Midbasin (m/s)
Spring tide	1.80	0.65	0.17
Mean tide	1.45	0.55	0.14
Neap tide	1.10	0.40	0.10

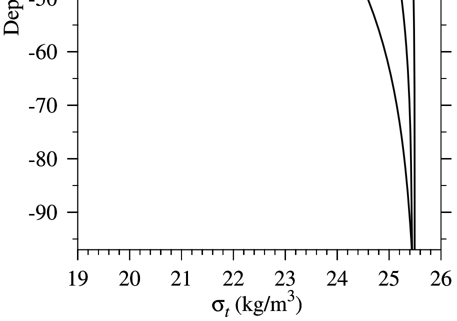

Figure 4. The initial density profiles represented for shallow, standard, and deep stratification cases. The model is initialized using these profiles with an assumption of no horizontal variation.

Table 2. Numerical Experiment Design[a]

Case	Tidal Forcing	Coriolis Force	MY-2.5	Constant Viscosity/Diffusivity	Bottom Friction	Standard Pycnocline	Shallow Pycnocline	Deep Pycnocline
S-SS	spring	×	×	√	√	√	×	×
M-SS	mean	×	×	√	√	√	×	×
N-SS	neap	×	×	√	√	√	×	×
M-SP	mean	×	×	√	√	×	√	×
M-DP	mean	×	×	√	√	×	×	√
S-C	spring	√	×	√	√	√	×	×
M-C	mean	√	×	√	√	√	×	×
N-C	neap	√	×	√	√	√	×	×
S-MY 2.5	spring	×	√	×	√	√	×	×
M-MY 2.5	mean	×	√	×	√	√	×	×
N-MY 2.5	neap	×	√	×	√	√	×	×
S-slip	spring	×	×	√	×	√	×	×
M-slip	mean	×	×	√	×	√	×	×
N-slip	neap	×	×	√	×	√	×	×

[a] Abbreviations are as follows: DP, deep pycnoclines; SP, shallow pycnoclines; SS: standard stratification; and S-C, M-C, and N-C, spring, mean, and neap tidal forcing cases with the Coriolis force. S-, M-, and N- are applied for MY level 2.5 and no bottom friction cases. Crosses indicate the absence of certain conditions, and the check signs indicate the presence of certain conditions.

ine the formation of the density depression resulting from the blocking of the stratified tidal flow over topography, we assume that the initial density (ρ) is linearly proportional to salinity (S):

$$\rho = 999.972 \times \left(1 + 0.75 \times 10^{-3} S\right). \tag{1}$$

The first suite of numerical experiments are focused on case studies with different intensities of tidal forcing (spring, mean and neap tidal amplitudes) (see Table 1) and stratification (shallow, standard, and deep) (Figure 4). The second set is derived from a process-oriented study that examines the influence of Coriolis force, turbulent mixing parameterization and bottom boundary conditions (Table 2). The mean tidal forcing here refers to the average amplitude of spring and neap tides. The results are validated by the comparison with MBIWE98 data and previous studies done by *Scotti et al.* [2007].

3. Model Results and Model-Data Comparisons

3.1. Wave Generation

[14] The model experiments indicate that internal waves over Stellwagen Bank are generated by a process during which an internal perturbation to the density field is formed by supercritical tidal flow over the topography and then maintained on the bank until it is subsequently released at the change of flow condition. For a given standard background stratification and spring tidal forcing, the model shows that starting from the ebb tide (about 1 h after the transition of tidal phase), a sharp density front gradually forms around the 30 m isobath at the western crest of Stellwagen Bank (500–600 m onbank from the slope) (Figure 5). Associated with this process, to the western side of the front the flow is strongly vertically sheared with eastward flow at the surface and weak westward flow at depth. To the eastern side of the front, a single massive depression (or lee wave) is generated and broadens in width over the eastern slope. The expansion of the depression is related to the development of a bottom-intensified jet current which originates from the density front and is generated when the lower layer of dense water, pushed up to the crest of the bank along the western slope, flows over the eastern slope. Away from the front region where the flow and topography interaction is much weak, the cross-bank circulation is dominated by the tide current. During the remainder of the ebb tidal period, the front remains quasi-stationary on the crest of the bank while the single massive depression has extended to a rather broad horizontal scale, reaching ~6 km near the bottom one hour before the transition of the tide from ebb to flood. At the eastern end of the depression, the near-bottom isopycnals raise up abruptly as a step.

[15] A time series of Froude numbers was calculated to see how the internal response of the density field is related to the variation of tidal flow on the bank. The Froude number is given as

$$F_r(z) = U(z)/c \tag{2}$$

where $U(z)$ is the cross-bank horizontal velocity and c is the first mode internal wave phase speed. The phase speed is computed on the basis of the model-produced density profile, using normal mode analysis (J. Klinck's Matlab program dynmodes.m, available online at http://woodshole.er.usgs.gov/operations/sea-mat/klinck-html/index.html). A plot of the first three vertical eigenmodes on the crest of the bank when the ebb tidal flow reaches the maximum velocity under standard stratification and spring tidal forcing is shown in Figure 6. The time series of the vertically averaged F_r over a tidal cycle at an upstream location (3 km west of the bank crest), on the bank crest and at a downstream location (6 km east of the bank crest) under the same conditions is shown in Figure 7. The F_r time series demonstrates that, around 1–2 h following the onset of ebb tide, the internal flow on the crest of the bank changes from subcritical to supercritical conditions near the location of the density front. The region of the supercritical flow then expands eastward with the development of the depression in the following hours until the ebb tide reaches the maximum intensity at which time the vertically averaged F_r on the crest of the bank is 1.6. Subsequently, the flow on the crest of the bank gradually transforms into subcritical condition near the time of slack tide, depending on the intensity of the tidal forcing. However, a near-bottom supercritical flow region still exists

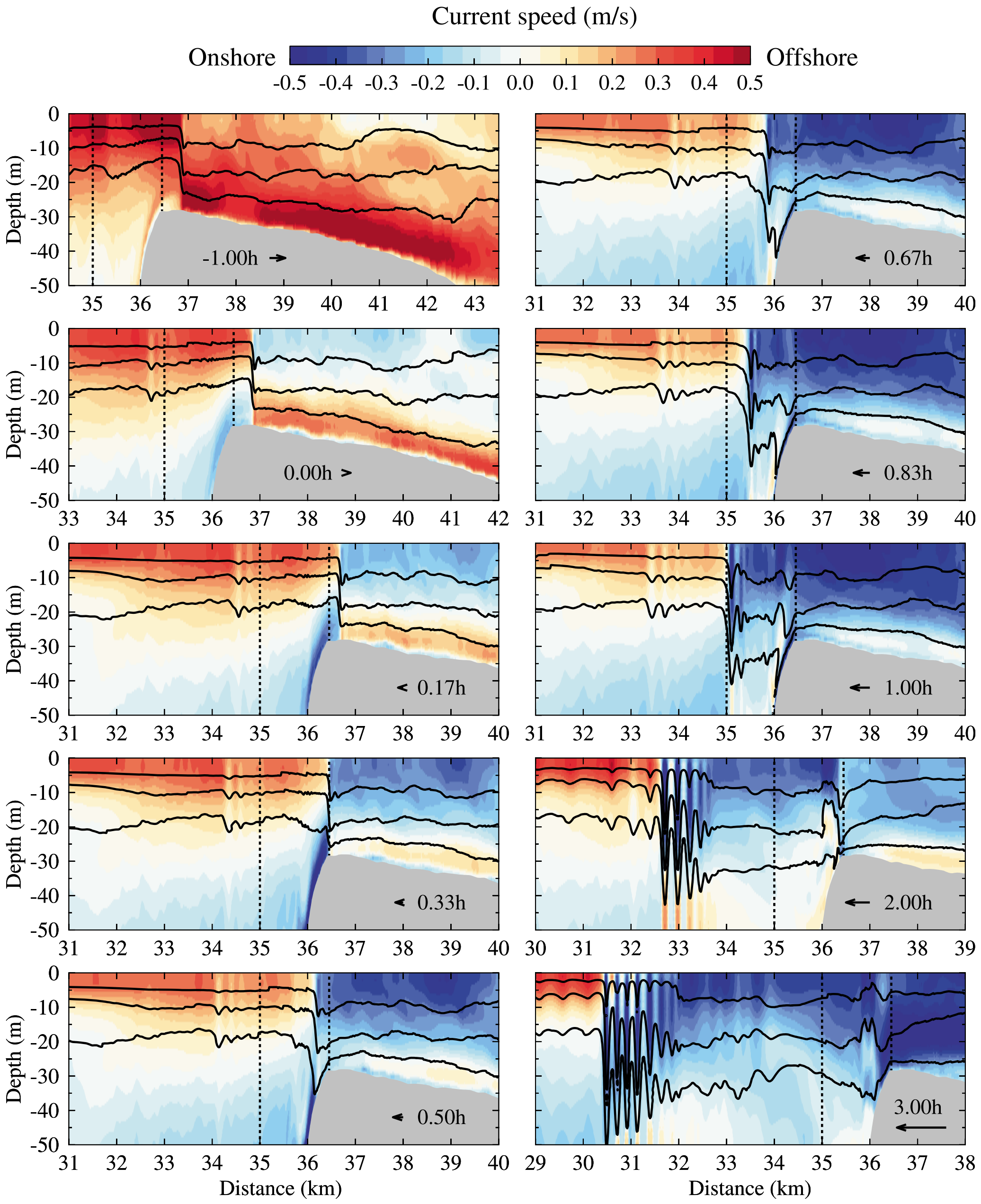

Figure 5. Snapshots of the cross-bank distribution of density contours σ_t = 22.5, 23.5, and 24.5 and cross-bank currents at −1.00, 0, 0.17, 0.33, 0.50, 0.67, 0.83, 1.00, 2.00, and 3.00 h relative to the ebb-flood transition for the standard stratification case driven by the spring tidal forcing. The negative sign indicates the ebb period. The ebb-flood transition is defined as the time of low tide at the open boundary. The area bounded by the two vertical dashed lines is the internal wave generation region during the flood tide.

and extends further downslope with the broadening of the depression. Overall, this result suggests that the formation of the density front and the variation of isopycnals over the eastern slope of Stellwagen Bank during the period of ebb tide are closely related to the change of tidal flow on the bank. This process is similar to the development of an internal hydraulic jump.

[16] During the transition from ebb to flood tide, the density front as well as the single massive depression starts to be advected westward. Although at this time the barotropic tidal current over the bank has turned to the onshore direction, the surface flow ahead of the front remains offshore and decreases exponentially westward away from the front (not shown). This is a feature in association with the wave of depression since the surface eastward flow only attaches to the leading edge of the generated internal wave and moves with it in the same speed. On the western slope, the near bottom westward flow is influenced by the frontal circulation so when the front propagates to the shelf break at 0.33 h in the flood period the flow reaches to the maximum

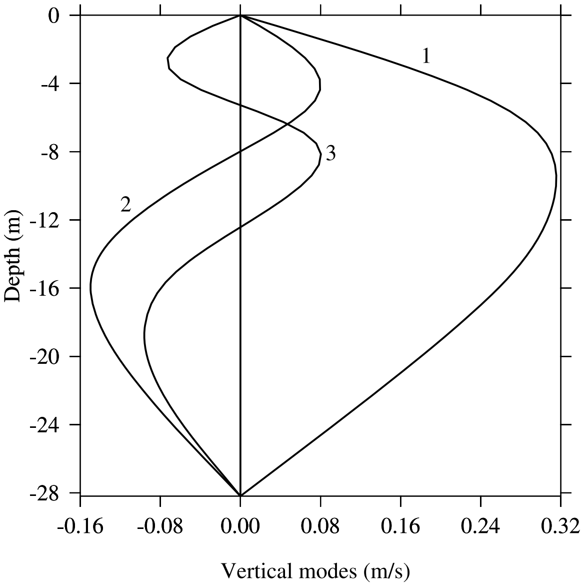

Figure 6. The first three vertical eigenmodes calculated using normal mode analysis (J. Klinck's Matlab program dynmodes.m) on the crest of Stellwagen Bank when the ebb tidal flow reaches the maximum under standard stratification and spring tidal forcing.

magnitude of ~0.5 m/s. When the density front moves onto the western steep slope half an hour later, the abrupt change in topography and the strong downward flow causes the front to steepen significantly and separate into two depressions: one trapped on the slope and the other moving westward off bank with the tidal current. The former is likely caused by the divergence of tidal flow over steep bottom topography [*Chen and Beardsley*, 1998]. The latter intensifies on its journey and is the seed of the large-amplitude nonlinear wave packet found in the observations. A careful examination of the free propagating depression at this stage shows that significant isopycnal steepening at the leading edge does not occur until the depression has reached the western edge of the steep slope region (indicated by the dashed lines). As suggested by *Scotti et al.* [2007], the rapid change in topography at the western steep slope actually counteracts the nonlinearity such that the depression is initially smoothed until reaching the western edge of the steep slope. This also indicates that dispersion (a nonhydrostatic effect) relative to nonlinearity is not important at the initial state of wave generation. In contrast, the single massive depression (lee wave) generated at ebb tide could not be advected over the bank and generate internal waves in the flood tidal period. As seen in Figure 5, it gradually levels off and disappears over the top of the bank. This result is actually similar to what has been found in the acoustic measurements of *Chereskin* [1983].

[17] The above described process of wave generation varies significantly with tidal forcing. When driving the model using the mean tidal forcing while maintaining the same background stratification, the model shows a density front and a broad depression 1 h before the transition of the tidal current (Figure 8). However, the cross-bank gradient of the front is much weaker and its location is shifted off bank of the slope. The vertically averaged Froude number on the crest of the bank reduces to 1.2 as the ebb tide reaches its maximum intensity. Similar to the spring tide case, the front separates into two distinct depressions in the early flood period, a topographically trapped and a free-propagating one. The well-defined internal wave packet develops in the interior region 3.5 km away from the western flank, which is about 0.5 km further west from the location in the spring tidal forcing case. This indicates that the wave is released earlier in association with the decrease of tidal forcing since the flow on the crest of the bank changes into subcritical at an earlier time. The intensity of the generated internal wave packet is relatively weaker in amplitude. As the forcing reduces to neap tide, the generation mechanism of internal waves remains qualitatively the same as those found in spring and mean tidal conditions (Figure 9). With weaker tidal forcing the vertically averaged Froude number on the bank crest has reduced to less than 1.0 during the entire ebb tide period, but the near-bottom supercritical flow region still exists. Since the front under such conditions can be released even earlier, the well-defined internal wave packet appears nearer to the coast, with significantly weaker amplitudes. Overall, reducing tidal forcing weakens the flow

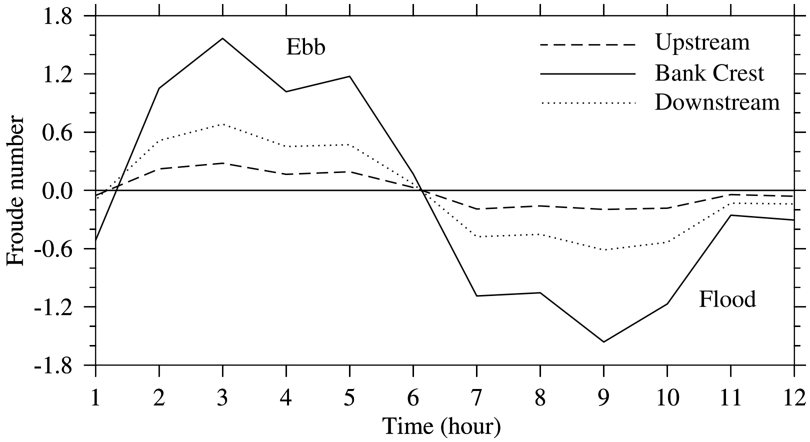

Figure 7. Time series of the vertically averaged F_r over a tidal cycle at an upstream location (3 km west of the bank crest) on the bank crest and at a downstream location (6 km east of the bank crest) under standard stratification and spring tidal forcing.

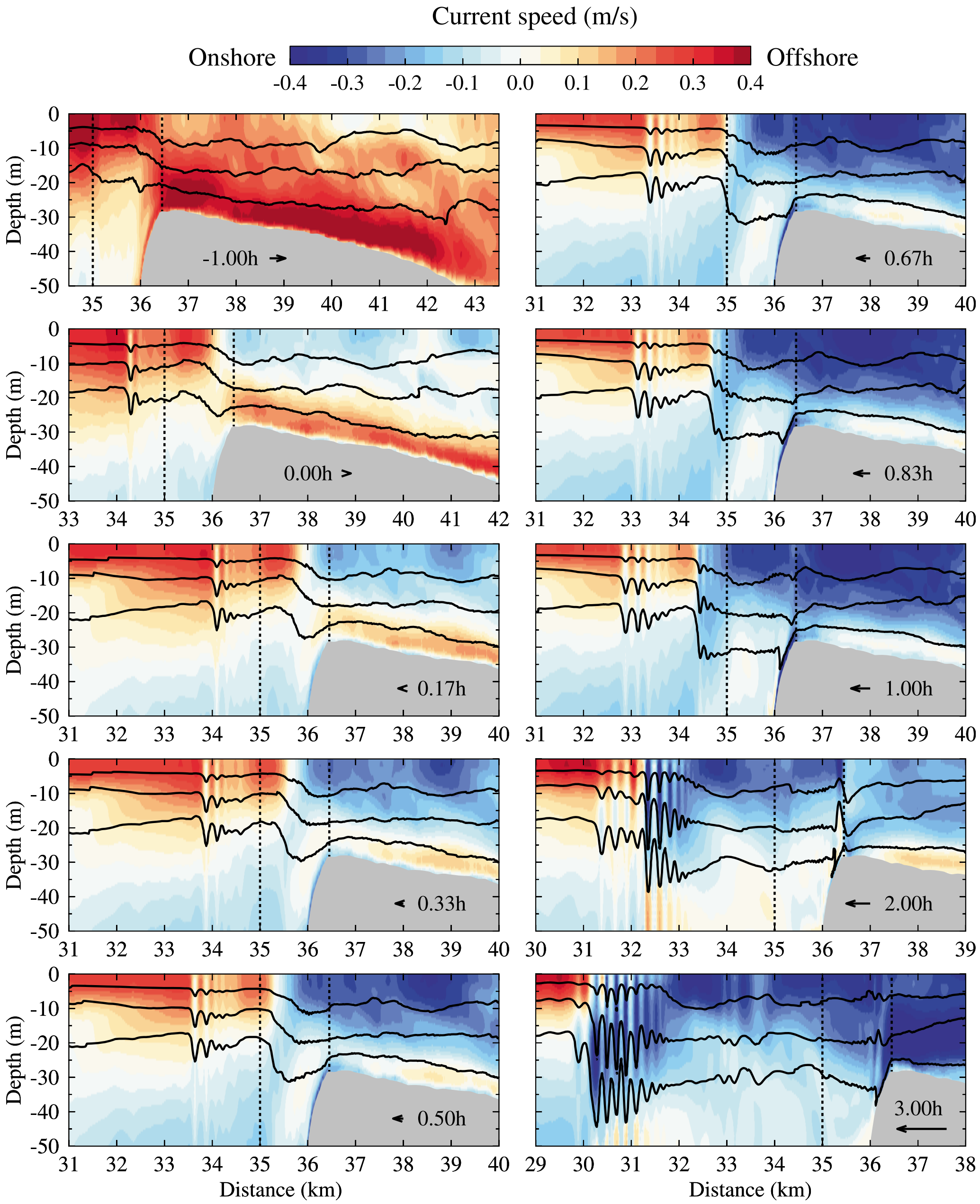

Figure 8. Snapshots of the cross-bank distribution of density contours σ_t = 22.5, 23.5, and 24.5 and cross-bank currents at select times relative to the ebb-flood transition for the standard stratification case driven by the mean tidal forcing. The selected hours and definition of ebb-flood transition are the same as those shown in Figure 5.

on the bank and results in an earlier transition from supercritical to subcritical conditions, which leads to an earlier released density perturbation with accordingly reduced amplitude.

[18] With mean tidal forcing, the timing and intensity of internal waves in shallow and deep pycnocline cases differ significantly from the standard stratification case. In the shallow pycnocline case, for example, a steep density front forms much more rapidly on the western side of the bank and a well-defined internal wave packet develops 1 km away from the western slope during the early stage of flood tide (Figure 10, left). The amplitude of the leading depression is also comparable to that from the spring tide case. In the deep pycnocline case, the model only shows a tiny density depression on the western flank of the bank around the ebb-flood transition. This depression gradually develops as it is advected toward the coast in the flood tidal period, and forms an internal wave packet 12 km away from the western slope about 5 h after the tidal currents turns to flood (Figure 10, right). This result is very similar to that observed in the neap tide case. The different responses of internal flow to stratification can be explained on the basis of the velocity pattern at the leading density depression. The vertical velocity, which is produced by the cross-bank tidal current

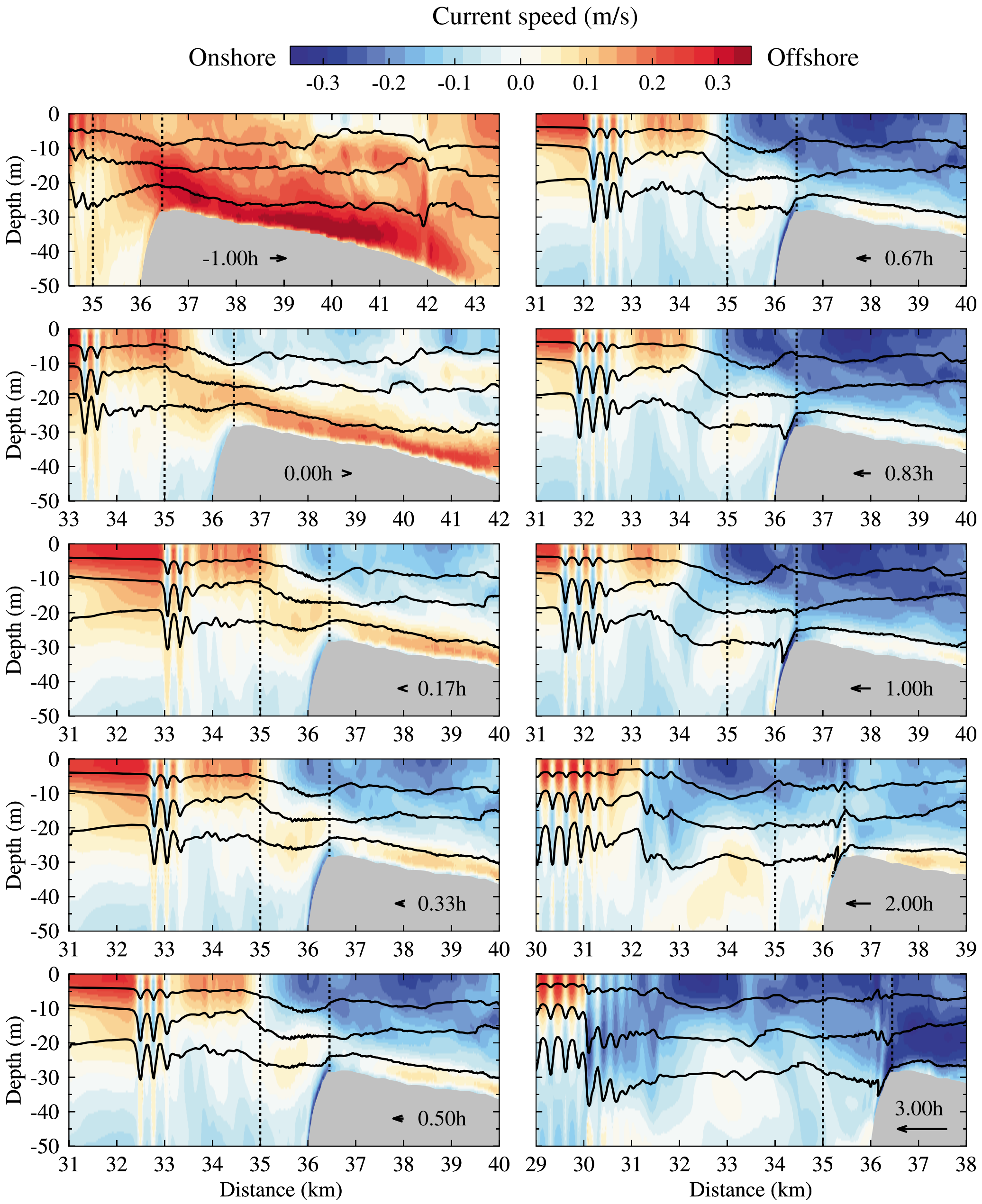

Figure 9. Snapshots of the cross-bank distribution of density contours σ_t = 22.5, 23.5, and 24.5 and cross-bank currents at select hours relative to the ebb-flood transition for the standard stratification case driven by the neap tidal forcing. The selected hours and definition of ebb-flood transition are the same as those shown in Figure 5.

convergence, has a much stronger influence on the depression of the isopycnals in the shallow pycnocline case when compared to the deep pycnocline case. Therefore, for a given tidal forcing at the eastern open boundary, the tidal-topographic interaction over the western slope of Stellwagen Bank acts as a stronger force in the shallow pycnocline case, which produces a deeper density depression. One can also link the resemblance between the shallow pycnocline case versus spring tidal forcing case and the deep pycnocline case versus neap tidal forcing case on the basis of the estimated Froude number. The vertically averaged Froude number on the bank crest in the shallow pycnocline case with mean tidal forcing is 1.8, even larger than the value of 1.6 in spring tidal forcing case, while the Froude number in the deep pycnocline case with mean tidal forcing is close to that in the neap tidal forcing case but less than the value in the standard stratification with mean tidal forcing case.

[19] It is worth mentioning that the model-computed results include a small-amplitude internal wave packet generated in the bayside region of the bank before the formation of significant internal wave packet (see Figures 5, 8, and 9). This wave packet is produced by the falling of the lifted pycnocline during the ebb tide. It appears in the standard stratification case but is not significant in shallow and deep

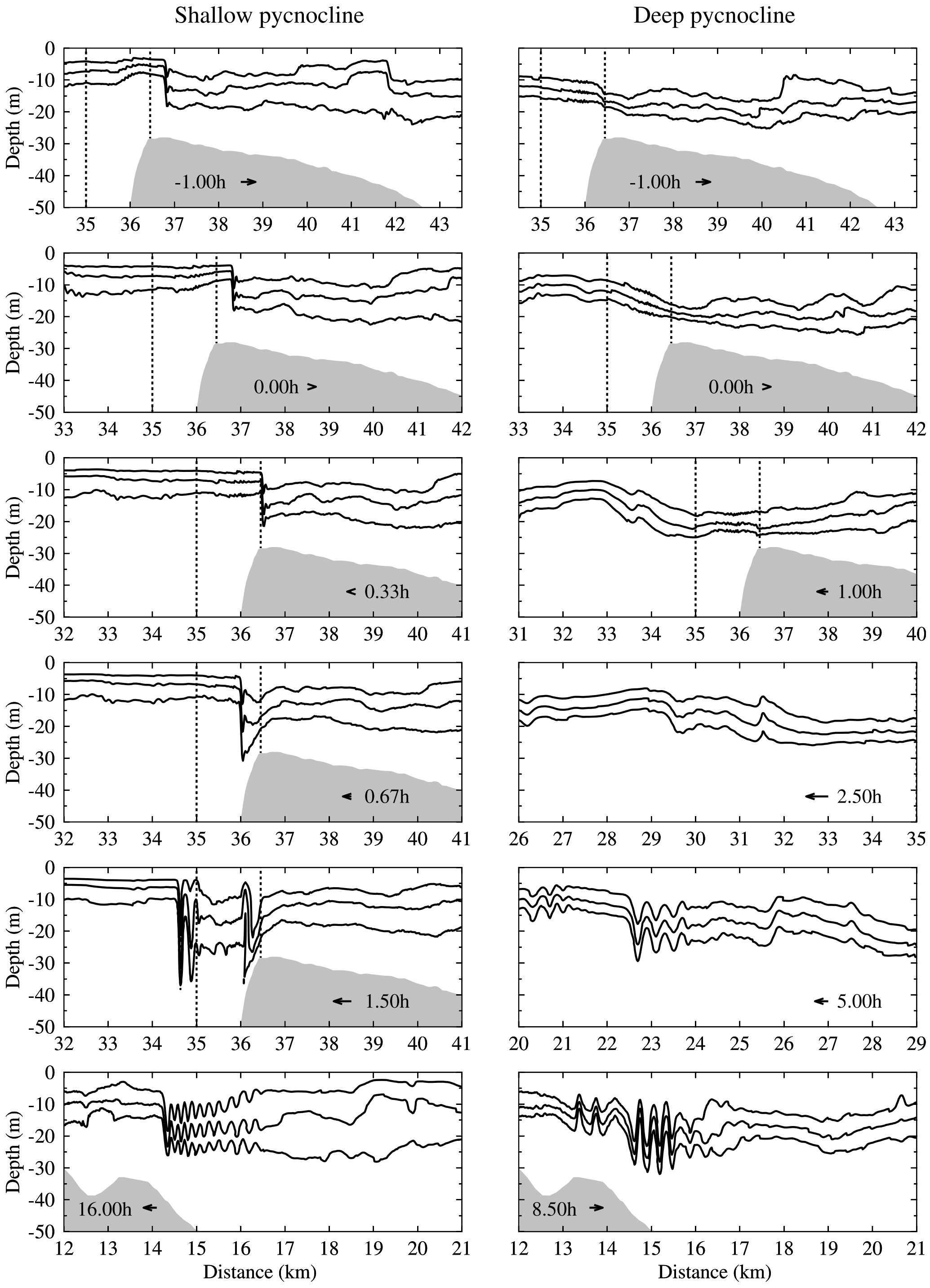

Figure 10. Snapshots of the cross-bank distribution of density contours at select hours relative to the ebb-flood transition for (left) shallow (σ_t = 24.0, 24.5, and 25.0) and (right) deep (σ_t = 21.0, 21.5, and 22) pycnocline cases driven by the mean tidal forcing. All time labels have the same definitions as those shown in Figure 5.

pycnocline cases, suggesting that the formation of these small-amplitude waves relies strongly on water stratification.

[20] Finally, the model results suggest that the generation of internal waves over Stellwagen Bank is exactly phase-locked to the M_2 tide, with two internal wave trains passing sites A, B and C over a 12 h time interval (normalized by the M_2 tidal period 12.42 h for simplicity) (Figure 11). In line with the observational data collected by *Butman et al.* [2006a, 2006b], the density variations at fixed water depths at the three sites show an abrupt jump when the wave packet arrives and then undergo a period of high-frequency oscillations persisting for 1–2 h.

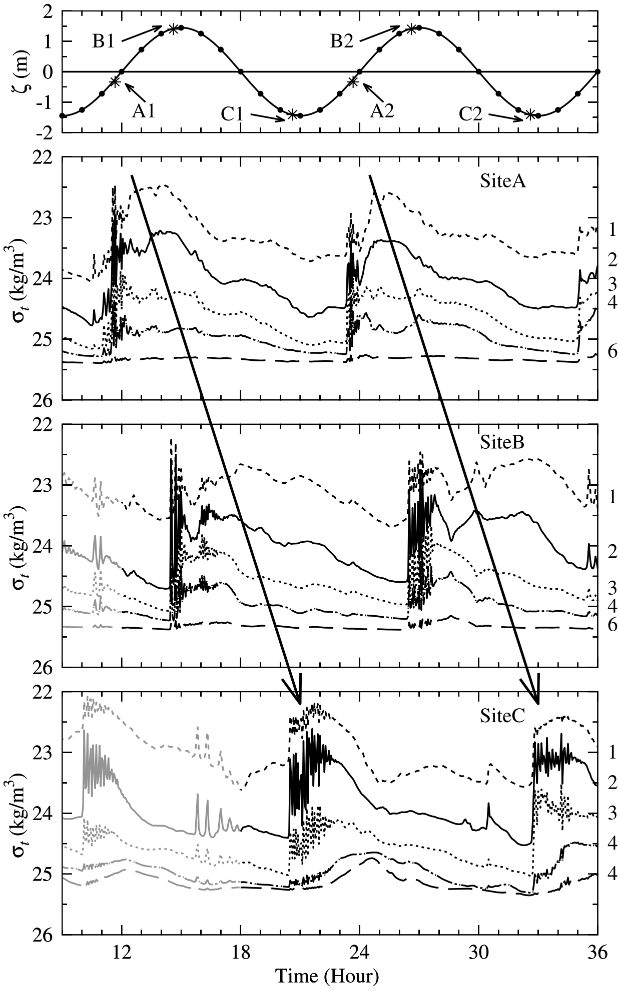

Figure 11. The first panel shows the time series of the M_2 surface elevation with marked times when the model predicted internal wave train arrives at observation sites A, B, and C. The second and third panels show the density time series at 10, 20, 30, 40, and 60 m at site A and site B, respectively. The fourth panel shows the density time series at 10, 20, 30, 40, and 45 m at site C during the M_2 tidal cycles. The gray color region in the time series at sites B and C is regarded as the results from model spin-up.

3.2. Wave Propagation, Shoaling, and Dissipation

[21] In the early flood tidal phase, the front has propagated away from the western steep slope region and evolves into a sizable amplitude depression. During propagation, the leading edge of the depression continuously steepens and the dispersion within the wave trough becomes increasingly important. Until the dispersion term is large enough to interplay with the nonlinear term at some point, undulations of the isopycnals appears behind the leading depression. At this time, the depression has evolved into an internal wave packet. This process is essentially consistent with the LB's descriptions for the second and final phase of wave generation. A theoretical explanation of the disintegration process has been described in previous works [LB; *Scotti et al.*, 2007]. Exactly when and where the depression is able to disintegrate into a well-defined wave packet is more or less determined by the "initial status" when the density front leaves the bank. For example, for spring tidal forcing, the late transition from supercritical to subcritical flow on the bank causes the delay of the density front entering the deep basin. But the stronger density front which is also related to larger Froude number on the crest causes it to quickly evolve into a large depression once entering the western steep slope. In contrast, for neap tidal forcing, the density front can be released much earlier while it has to undergo a significantly longer time to evolve into a well-defined internal wave packet. For shallow and deep pycnocline cases, the similar difference during wave propagation is also visible as comparing Figure 8 with Figure 10.

[22] In our simulations, the propagation speed of the internal wave was found to be insensitive to the intensity of tidal forcing but varied significantly with stratification. For example, from site A to site B, the average propagation speed in the standard stratification case is 0.57 m/s for the spring tide and 0.56 m/s for mean and neap tide cases (Table 4). These speeds decrease by ~0.12 m/s from site B to site C, implying a shoaling of the internal wave train as it travels toward the coast (Table 5). In the shallow pycnocline case, the average propagation speed between sites A and B is quite slow, 0.34 m/s, with a slight increase to 0.39 m/s between sites B and C.

[23] The model-computed velocity structure within the internal wave trains for the various test cases is qualitatively similar. As an example, the velocity field within a wave train in the standard stratification case driven by spring tide forcing (Figure 12) is characterized by a first-mode pattern in the vertical. The vertical velocity due to the horizontal flow convergence at the leading edge of the first wave can be as large as 0.2 m/s with a vertical internal density displacement of ~20–30 m. The resulting near-surface convergence and divergence of the horizontal velocity can modify the free surface roughness and produce a banded pattern that can be observed in satellite images and surface radar.

[24] The high-frequency internal wave packet propagates toward the coast without significant dissipation until it shoals over the nearshore slope of Massachusetts Bay around the 35 m isobath. In this region, the leading density depression of the wave train is comparable to the local water depth. In all cases, the model shows that the isopycnals containing the bottom water are compressed as the wave approaches the topography (Figure 13). As a result, a strong offshore current with high-frequency cross-isobath variation appears near the bottom. The magnitude and extent of this offshore current varies with the intensity of the incoming internal waves. For example, in the standard stratification case, the wave train generated by spring tidal forcing is more energetic than those driven by mean and neap tidal forcing with deeper depressions nearly reaching the bottom. In this case, the offshore flow extends over the entire bottom of the slope region (~5–6 km), with a maximum velocity of >0.3 m/s (Figure 13, top). The pattern of the cross-isobath high-frequency variation in the near-bottom offshore flow is determined by the number of high-frequency wave peaks, which is greater in the mean tidal forcing case than in spring and neap tidal forcing cases (Figure 13, middle and bottom). In all cases, this strong wave and topography interaction process breaks the well defined wave packet such that part of

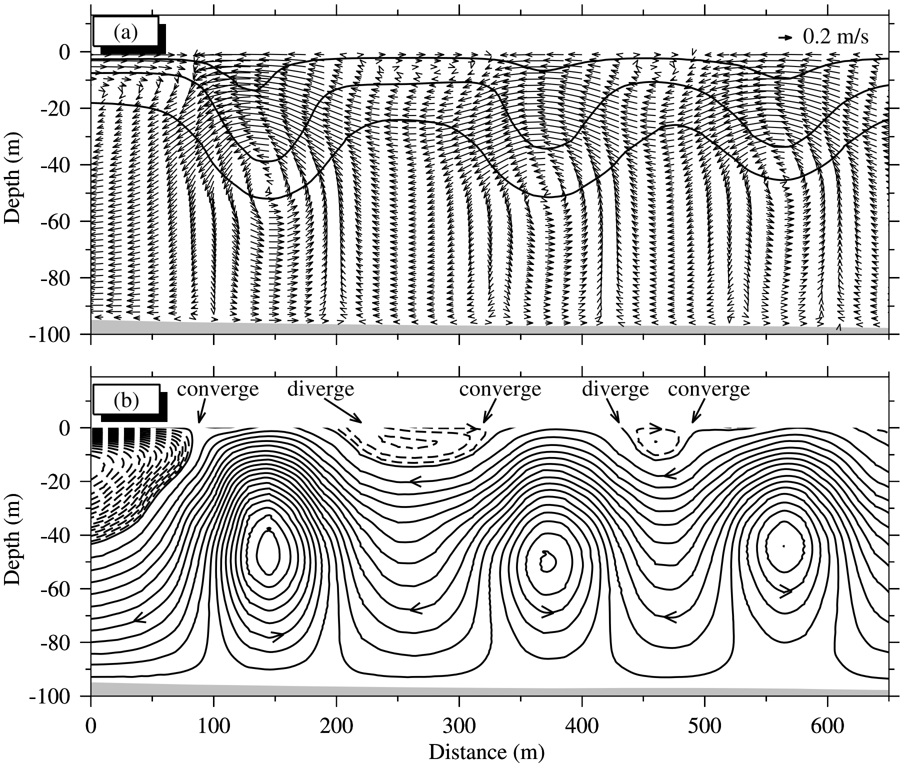

Figure 12. Velocity field overlapped with (a) density contours σ_t = 22.5, 23.5 and 24.5 and (b) stream function contours within a typical internal wave train. A single solitary wave is characterized by a counterclockwise cell (solid line). The near-surface flow between two solitary waves is characterized by clockwise cells with surface convergence/divergence. The stream function is plotted using a contour interval of 0.2 for clockwise cells (dashed lines) and 1.0 for counterclockwise cells (solid lines).

the wave transforms into another form propagating further onshore and part of the wave is lost to the mixing process. This result is consistent with the modeling analysis of *Scotti et al.* [2008].

3.3. Effects of Rotation, Bottom Friction, and Vertical Diffusion

[25] Previous models used to study the physics of internal waves in Massachusetts Bay were based on the solution of inviscid equations and thus could not properly include the influence of bottom friction and vertical diffusion in a nonrotational system. Experiments were made in the present work to investigate the impact of bottom friction, vertical diffusion and Earth's rotation on wave evolution. The examples given here are for the standard stratification case driven by spring tidal forcing. We found that in comparison with the nonrotational case, Earth's rotation causes two distinct features during wave generation and propagation. First, the intensity of the density front on the crest and the subsequently formed depression on the western slope of Stellwagen Bank is weaker. Second, the wave propagates faster. As shown in Figure 14, the cross-bank scale of the density front near the ebb-flood transition is about 1 km in the case with rotation, while it is only 0.1 km in the case without rotation (Figure 5). The cause of this is that Earth's rotation transfers part of the tidal flow to the along isobath direction which leads to a reduction of the Froude number on the bank. For the same reason, the density depression, which forms as the front is advected off bank, becomes weaker. Leaving the western steep slope region, the density depression disintegrates into a well-defined wave train in a manner similar to the nonrotational case. In comparison, rotation seems to have little influence on the amplitude of the generated wave. This may be because the magnitude of isopycnal displacement is more dominated by the stratification if the forcing conditions remain the same. However, rotation has the effect of enlarging the wavelength and thus wave period, since the rate of energy input from the surface tide acting on depressing the leading edge of the isopycnals is reduced by the transfer of energy into the transverse direction.

[26] Bottom friction also has significant influence in the wave evolution. The major difference is observed in the cross-bank scale of the density front on the western flank of Stellwagen Bank, which is ~1.2 km near the ebb-flood transition (Figure 15), much larger than that observed in the case with bottom friction (Figure 5). Owing to the inviscid conditions, the location of the front is shifted eastward about 0.5 km. In the early stage of flood tide, the downward flow over the western steep slope is unconstrained by the absence of bottom friction. This enhances the nonlinearity, so that the freely propagating depression moves off bank more rapidly. When it leaves the steep slope region, a larger amplitude depression is formed in the inviscid case with a 5 m increase in vertical displacement of the isopycnals. Correspondingly, the subsequently generated internal wave train is characterized by a shorter wavelength. When these waves shoal over the nearshore slope of Massachusetts

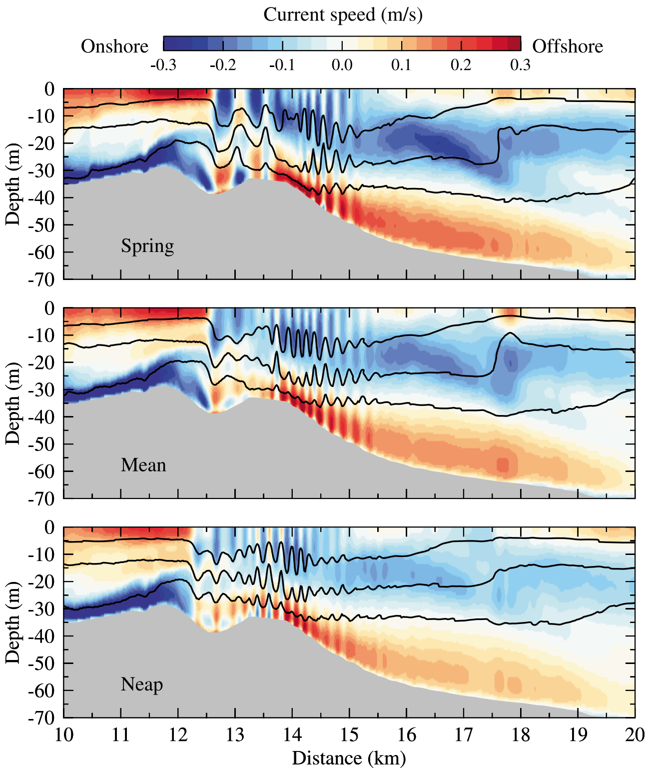

Figure 13. Snapshots of the density contours σ_t = 22.5, 23.5, and 24.5 and cross-isobath velocity image over the inner slope of Massachusetts Bay where the internal wave train shoals for the standard stratification cases driven by spring, mean, and neap tidal forcing. Colors indicate the magnitude of the velocity offshore (positive) and onshore (negative).

Bay, the wave breaking process is qualitatively similar but the local dissipation is smaller when compared with the frictional case (Figure 13).

[27] With the MY 2.5 turbulent parameterization enabled, the model-computed wave evolution is quantitatively similar to the baseline case with fixed background eddy viscosity. The calculated eddy viscosity within the wave train is similar to the value of background mixing 10^{-5} m^2/s in the model. This value is found at the same order of diapycnal diffusivity of 2.5 × 10^{-5} m^2/s within the wave packet which can be derived on the basis of the estimated dissipation rate of 2.6 × 10^{-6} W/kg found in the MBIWE98 measurement [*Scotti et al.*, 2006]. Only when the internal wave interacts with the topography such as during wave generation at the western slope of Stellwagen Bank and wave breaking over the nearshore slope of Massachusetts Bay does the model produce small patches of significantly increased value of eddy viscosity of the order of 10^{-1}–10^{-3} m^2/s near the bottom.

3.4. Model-Data Comparison

[28] *Butman et al.* [2006a, 2006b] provided a detailed characterization of the internal wave packets observed at sites A, B and C during MBIWE98. With time referenced to low tide at site B (t = 0), the wave packet arrived at site A around t = 2.1 ± 0.3 h, at site B around t = 5.2 ± 0.5 h (the last hour of the flood tide), and at site C around t = 10.0 ± 1.1 h (near the end of ebb tide). The average propagation speed between sites A and B was 0.63 m/s and between sites B and C was 0.54 m/s (with no correction made for advection). Within a wave packet, there were 5–10 internal waves with a wavelength of 200–400 m and a period of 5–10 min. As the wave packet arrived at the measurement sites, it caused a downward depression of the thermocline of ~30 m and high-frequency oscillations that lasted for 1–2 h.

[29] Statistics of the internal waves simulated in our case studies are summarized in Tables 3, 4, and 5 (the model setup for each case is listed in Table 2). Generally speaking, the model captures the characteristics of the observed internal wave packet and internal wave (IW) development processes at these three sites. In particular, in the cases with standard stratification, spring, mean, and neap tidal forcing and no rotation, the model-predicted wavelength, wave period, duration time and number of internal waves are 220–380 m, 6.7–12 min., 1.0–2.0 h and 7–14 internal waves at the three sites. These values are generally within the observational range. In these three cases, the internal wave propagation speed is 0.56–0.57 m/s at site B and drops to 0.45–0.46 m/s at site C, which are slower than the observed speeds by 0.06 m/s at site B and 0.09 m/s at site C.

[30] Tables 3–5 show that the internal wave characteristics vary significantly with initial pycnocline structure, Earth's rotation and bottom friction. The internal wave packet propagates slower (faster) with a shallow (deep) pycnocline. Earth's rotation causes an increase in the internal wave propagation speed to 0.60–0.68 cm/s at site B and 0.56–0.59 cm/at site C, which are better agreement with the observations. The wave speed predicted in the case without bottom friction is similar to that shown in the constant eddy viscosity case with bottom friction, which suggests that bottom friction has minor effects on the propagation of the internal wave, although it does have significant effects during wave generation and dissipation.

[31] The MBIWE98 measurements detected a relatively strong near-bottom downslope current (~0.4 m/s) over the offshore slope of western Massachusetts Bay, when the observed internal wave packet passed by. This feature is quantitatively captured in our experiments with or without rotation and/or bottom friction, but differences exist between the case with and without rotation. For example, at site B, in the case with Earth's rotation (Figure 16), the near-bottom offshore current abruptly occurs with a peak speed of ~0.2 m/s, while it appears before the arrival of the internal wave packet and continues to increase from ~0.1 m/s to >0.3 m/s during the wave shoaling as observed at site C (Figure 16). This feature found in the rotation case looks more similar to the observations (Figure 16, top).

4. Discussion

[32] LB and *Maxworthy* [1979] proposed two different mechanisms for internal wave generation over Stellwagen Bank. The major discrepancies between LB and Maxworthy's explanations are when and where the internal waves are produced. LB's theory suggests that the initial temperature front is generated during the early stage of flood tide on the western side of the bank. In contrast, Maxworthy's theory proposes that the internal wave is the result

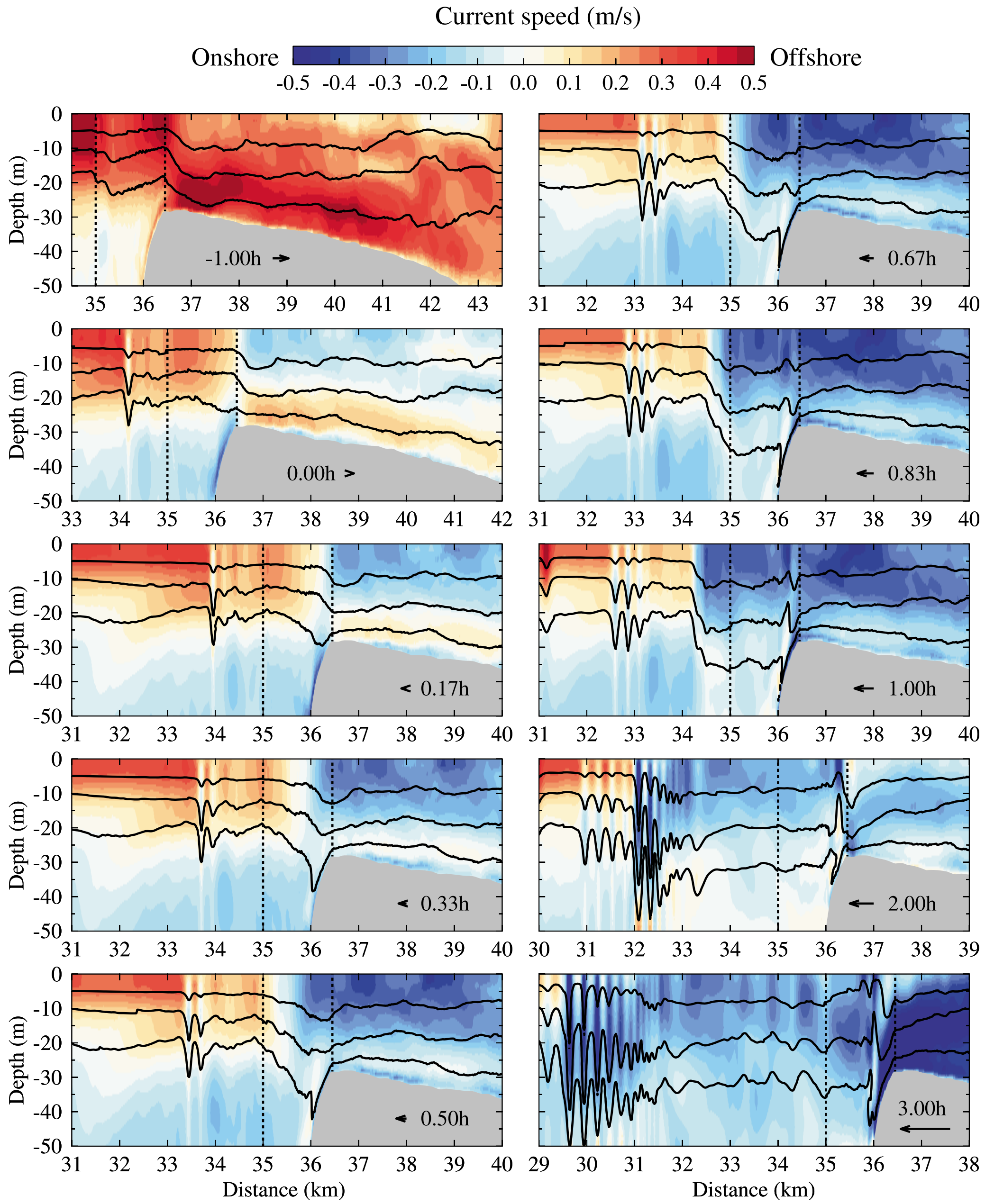

Figure 14. Snapshots of the cross-bank distribution of density contours σ_t = 22.5, 23.5, and 24.5 and cross-bank currents at the selected hours relative to the ebb-flood transition for the standard stratification and spring tidal case with inclusion of Earth's rotation. The selected hours and definition of ebb-flood transition are the same as those shown in Figure 5.

of the disintegration of a single lee wave created in previous ebb tide as it propagates upstream over the topography during the onset of slacking tide. Our numerical experiments reproduce three distinct phases of internal wave generation that are consistent with LB's descriptions. In addition, similar to the results of numerical simulation by *Scotti et al.* [2007], our modeling studies further show that the temperature front described in the first phase of LB's generation mechanism originates from a density perturbation initialized and maintained on the crest of the bank during the previous ebb tide. Our current numerical experiments show the distinct response and fate of the density perturbation with the ebb tide lee wave during the process of wave generation which is the key that supports the generation mechanism proposed by LB but not by Maxworthy.

[33] In none of the conditions represented by our test cases do we find that the internal depression generated from the lee side (eastern flank) of the bank propagates across the bank and disintegrates on the western slope as suggested in *Maxworthy*'s [1979] experiment. Instead, the model shows small-scale eastward propagating internal waves which are probably generated as a result of the upstream propagation of the density depression on the western flank during the ebb tide (not shown). This feature is similar to the process

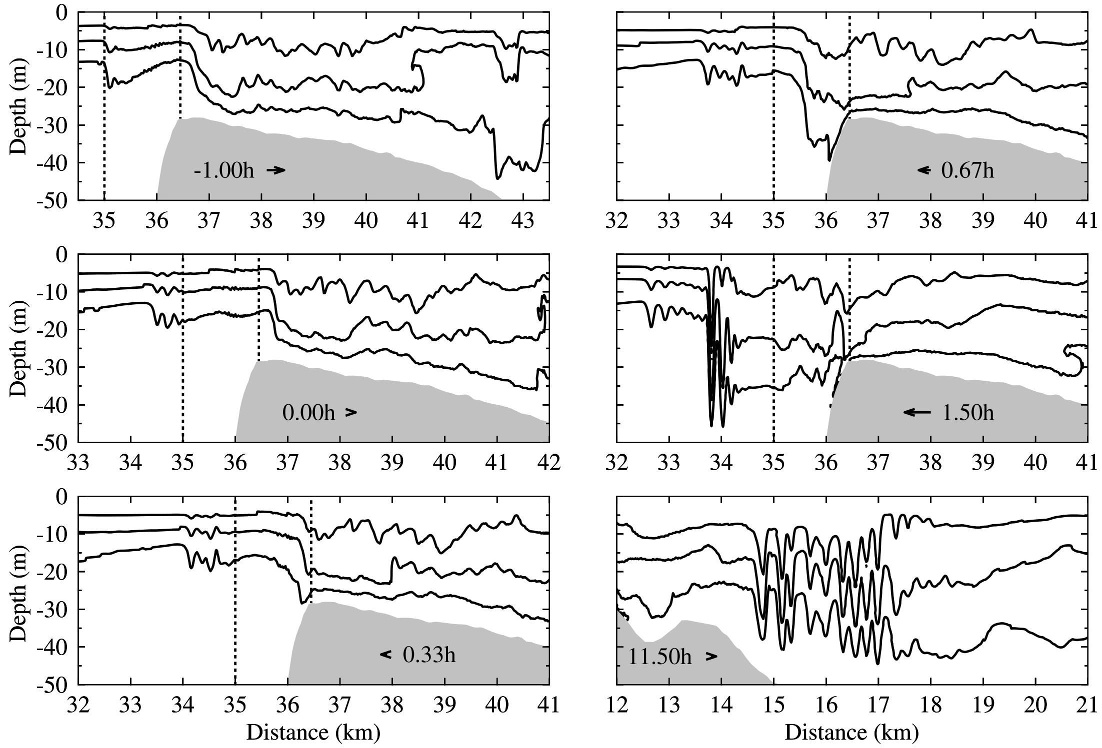

Figure 15. Snapshots of the cross-bank distribution of density contours $\sigma_t = 22.5$, 23.5, and 24.5 at the selected hours relative to the ebb-flood transition for the standard stratification and spring tidal case with no bottom friction. All time labels have the same definitions as those shown in Figure 5.

suggested by Maxworthy if one considers the western flank to be the lee side of the bank for the flood tide. This begs the question of why the internal depression on the eastern slope is unable to propagate across Stellwagen Bank into Massachusetts Bay. One possibility is that the eastern slope of Stellwagen Bank is too wide. To test this hypothesis, we repeated our experiments using an idealized symmetric bank case with a width of ~2 km, about 10 times narrower than that of Stellwagen Bank.

[34] Our symmetric bank experiment shows that the generation process of internal waves does not seem to change as the width of the bank is reduced. An example is shown in Figure 17 for the spring tide case with standard stratification. The model does show a deep density depression on the lee side, like that observed in *Maxworthy*'s [1979] experiment near the ebb-flood transition. At the same time, however, a sharp density front also forms on the top of the bank as noted in the case with realistic Stellwagen

Table 3. Statistical Characteristics of Model-Predicted Wave Packets at Site A[a]

Case	Maximum Depression (m)	Timing[b] (h)	Wavelength (m)	Wave Period (min)	Duration[c] (h)	Number of Internal Waves in a Passing Packet
S-SS	30	2.76	220	6.7	1.0	7
M-SS	25	2.65	221	6.9	1.0	8
N-SS	15	2.59	282	10.0	1.7	7
M-SP	35	2.82	260	10.0	1.2	5
M-DP	NA	NA	NA	NA	NA	NA
S-C	29	2.44	289	6.9	0.9	7
M-C	22	2.36	270	7.0	0.9	8
N-C	13	2.33	289	10.0	1.0	6
S-MY2.5	28	2.90	235	6.8	0.9	7
M-MY2.5	22	2.70	235	6.9	0.9	6
N-MY2.5	12	2.60	266	8.6	1.4	5
S-slip	38	2.76	224	5.2	0.8	7
M-slip	27	2.53	221	6.9	0.7	6
N-slip	15	2.53	269	10.0	1.8	10

[a] Case abbreviations are the same as in Table 2. NA, not available.

[b] Time is in real hours and relative to the ebb-flood transition, or equivalent to the beginning of flooding tide.

[c] The period of high-frequency pycnocline oscillations is counted when an internal wave packet passes the observational site.

Table 4. Statistical Characteristics of Model-Predicted Wave Packets at Site B[a]

Case	Maximum Depression (m)	Timing[b] (h)	Wavelength (m)	Wave Period (min)	Duration[c] (h)	Number of Internal Waves in a Passing Packet	Local Propagate Speed (m/s)	Average Propagate Speed From A to B (m/s)
S-SS	28	5.80	241	10.0	2.0	7	0.55	0.57
M-SS	26	5.69	366	12.0	2.0	8	0.56	0.56
N-SS	23	5.69	380	10.6	2.0	6	0.55	0.56
M-SP	17	8.97	250	10.0	2.2	6	0.33	0.34
M-DP	12	4.34	375	8.3	0.6	3	0.73	NA
S-C	26	5.00	370	10.0	2.0	10	0.66	0.68
M-C	24	4.95	414	10.0	2.0	11	0.66	0.68
N-C	18	5.06	356	10.0	2.5	8	0.62	0.60
S-MY2.5	26	5.92	266	6.9	2.0	6	0.54	0.58
M-MY2.5	25	5.78	378	12.0	1.9	6	0.53	0.57
N-MY2.5	23	5.75	368	10.4	2.0	7	0.54	0.55
S-slip	30	5.77	235	6.9	1.7	9	0.57	0.58
M-slip	25	5.61	260	6.9	1.9	12	0.56	0.57
N-slip	20	5.64	347	11.0	1.7	9	0.56	0.56

[a] Case abbreviations are the same as in Table 2. NA, not available.
[b] Time is in real hours and relative to the ebb-flood transition, or equivalent to the beginning of flooding tide.
[c] The period of high-frequency pycnocline oscillations is counted when an internal wave packet passes the observational site.

Bank bathymetry. As the tidal current turns to the flood phase, the density front moves faster to the western slope and disintegrates into an internal wave packet owing to nonlinear interaction with the topography. The density depression found on the lee side of the bank also propagates westward in the early flood tide and forms a sharp gradient in the isopycnals. However, this depression moves so slowly that the well-defined internal wave packet is found on the western side of the bank before its arrival. The result essentially repeats our previous conclusion that although a single massive density depression (lee wave) could be formed on the lee side during ebb tide, it is the relaxation of the density perturbation or front on the bank crest instead of the lee wave that contributes to the observed large-amplitude, high-frequency nonlinear internal waves found on the western side of Stellwagen Bank.

[35] Earth's rotation is often ignored in the study of tide topography–generated high-frequency internal waves. Our case studies show that the tidal rectification process which transfers part of cross-bank tidal kinetic energy into the along-bank direction via bottom friction and Coriolis force can significantly affect internal wave generation. This energy transfer as indicated by the reduced Froude number weakens the intensity of the density front formed on the bank crest at the ebb-flood transition and also the density depression on the western slope in the early phase of flood tide. Figure 18 shows the vertically integrated cross-bank total kinetic energy at three select times relative to the ebb-flood transition for the cases with and without Coriolis force. The along-bank energy transfer due to the influence of Coriolis force causes a reduction of the cross-bank total energy by a factor of ~25%. The divergence of the cross-bank momentum in the along-bank direction can lead to the formation of the along-bank residual current jet of ~10 cm/s on the western flank. This tidal rectification process is the

Table 5. Statistical Characteristics of Model-Predicted Wave Packets at Site C[a]

Case	Maximum Depression (m)	Timing[b] (hour)	Wavelength (m)	Wave Period (min)	Duration[c] (h)	Number of Internal Waves in a Passing Packet	Average Propagate Speed From B to C (m/s)
S-SS	15	12.02	270	10.0	2.0	11	0.45
M-SS	13	11.96	202	7.0	2.0	14	0.45
N-SS	11	11.67	270	10.0	1.9	10	0.46
M-SP	12	16.10	154	5.5	1.7	10	0.39
M-DP	12	8.51	298	12.0	1.3	5	0.66
S-C	15	9.95	365	13.0	2.2	7	0.56
M-C	15	9.89	400	17.0	1.7	6	0.56
N-C	13	9.72	452	16.0	2.0	6	0.59
S-MY2.5	13	12.13	296	12.1	1.9	9	0.44
M-MY2.5	13	12.08	214	10.4	2.1	11	0.44
N-MY2.5	11	11.76	235	10.1	1.7	10	0.46
S-slip	15	11.73	280	12.0	2.0	11	0.46
M-slip	13	11.67	212	9.0	2.2	14	0.45
N-slip	12	11.50	269	10.0	2.1	11	0.47

[a] Case abbreviations are the same as in Table 2.
[b] Time is in real hours and relative to the ebb-flood transition, or equivalent to the beginning of flooding tide.
[c] The period of high-frequency pycnocline oscillations is counted when an internal wave packet passes the observational site.

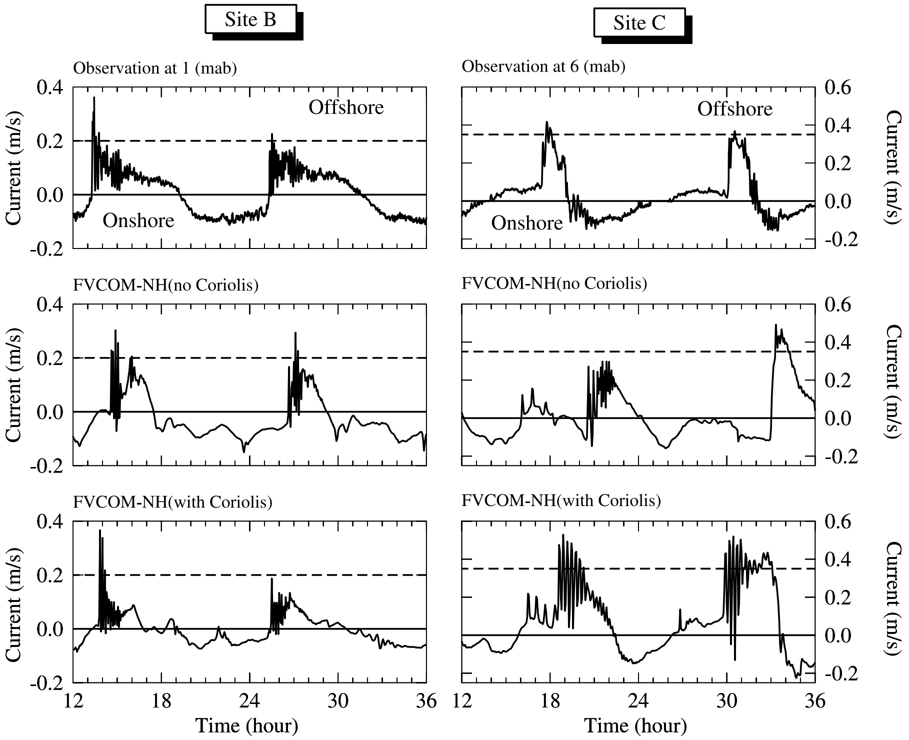

Figure 16. Comparison of model-predicted and observed near-bottom velocities at sites B and C for the standard stratification and spring tidal case without and with Coriolis force. Observational data provided by B. Butman (U.S. Geological Survey).

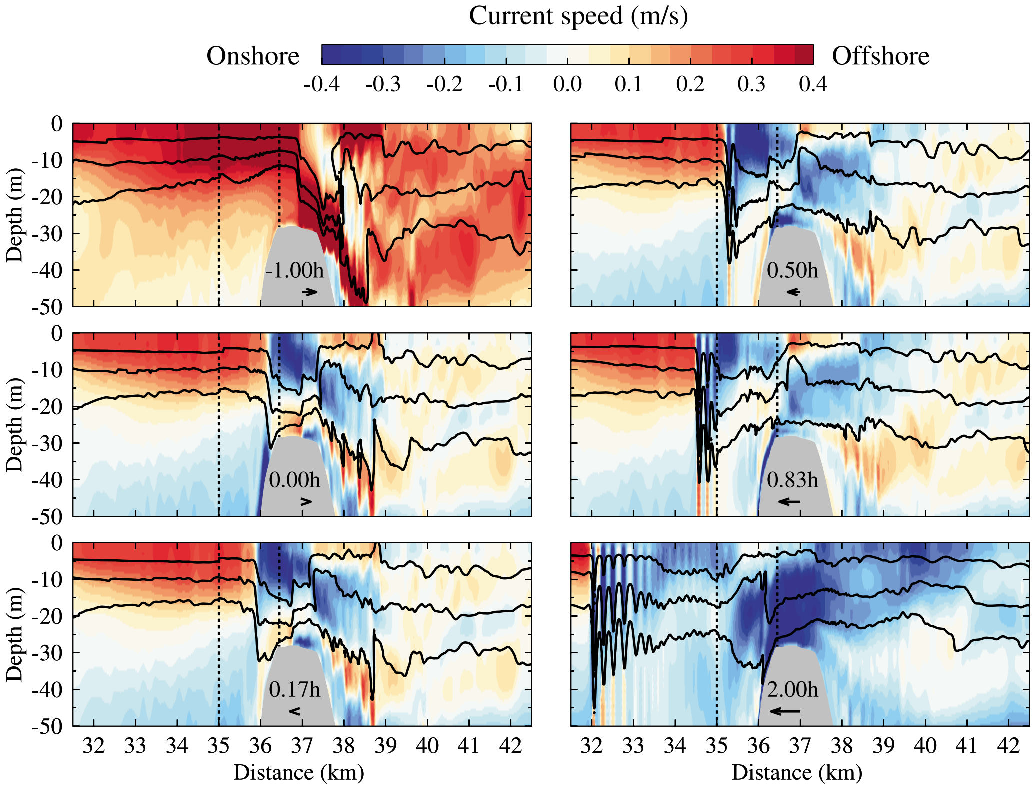

Figure 17. Snapshots of the cross-bank distribution of density contours σ_t = 22.5, 23.5, and 24.5 and cross-bank currents at select hours relative to the ebb-flood transition for a symmetric bank case initialized with standard stratification and driven by spring tidal forcing. All time labels have the same definitions as those shown in Figure 5.

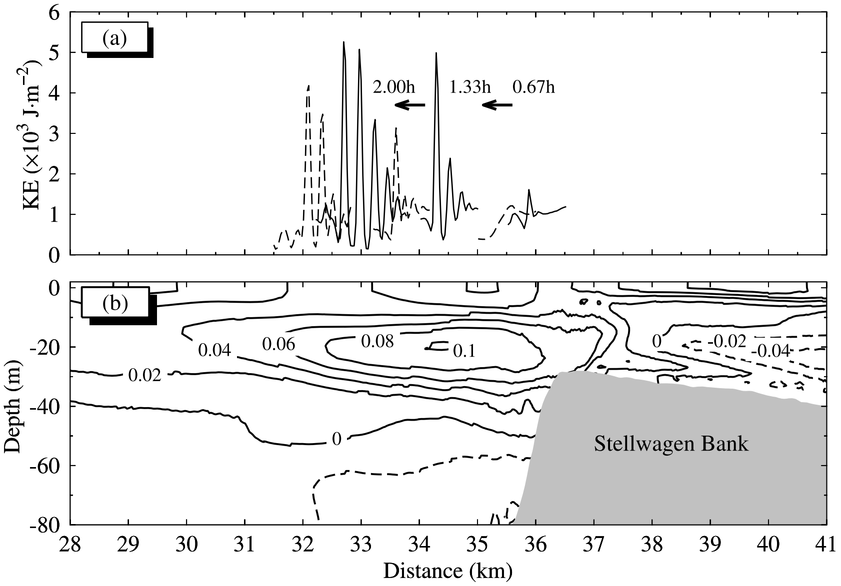

Figure 18. (a) Distribution of vertically integrated kinetic energy of the cross-bank flow within the early developed and mature internal wave packets at 0.67, 1.33, and 2.00 h relative to the ebb-flood transition for the case without (solid line) and with (dashed line) Coriolis force. (b) Cross-bank distribution of along-bank residual velocity. The experiment is conducted for the case initialized with standard stratification and driven by the spring tidal forcing.

same as that found over Georges Bank [*Loder*, 1980; *Chen and Beardsley*, 1995].

[36] Another significant influence of Earth's rotation on high-frequency internal waves in Massachusetts Bay is the increased propagation speed (see Figure 18 and Tables 3–5). The comparison between the hydrostatic and nonhydrostatic experiments suggests that the westward propagating internal wave train is a leading edge feature of the internal tidal wave, so that the propagation speed of the wave packet is mainly the same as the internal tidal wave. *Gerkema* [1996] studied the effect of Earth's rotation on the internal tides and internal waves in an idealized two-layer fluid system and suggested that the long internal wave phase speed in a rotating system can be expressed by

$$c_f^2 = \frac{c_o^2}{1 - f^2/\omega^2} \tag{3}$$

where c_o is the phase speed of the linear long internal wave without rotation, f is the Coriolis frequency and ω is the tidal angular frequency. Massachusetts Bay is dominated by the M_2 tide. Given the value of f at 42.2°N, $f/\omega \sim 0.697$. Therefore,

$$c_f \sim 1.39 c_o \tag{4}$$

The ratio of c_f/c_o in our experiments for the standard stratification case is 1.1–1.2 from site A to site B and 1.2–1.3 from site B to site C, which is close to the value given in (4). Considering the effects of friction and stratification, we conclude here that the faster speed found in the case with Coriolis force is a result of the rotation-induced increase of the propagation speed of the internal tidal wave.

[37] Our case studies also suggest that the intensity, propagation and shoaling of the internal wave train are significantly influenced by bottom friction. Although the basic features of the wave packets remain the same without bottom friction, the details of the wave generation process and the resulting characteristics of the wavelength, period and number of internal waves in a packet are found to be different. Moreover, bottom friction can act together with the Coriolis force on tidal rectification that provides a further modification of the wave generation process. On the contrary, our test cases with MY level 2.5 turbulent closure scheme show that internal wave–induced vertical mixing is small such that only a marginal effect is found on wave generation and propagation. However, since the model grid is still not high enough to resolve the localized strong mixing process such as shear induced wave breaking within a wave packet as found in acoustic data, further investigation on this topic is needed.

5. Conclusions

[38] Large-amplitude, high-frequency, nonlinear internal waves are a major dynamical feature observed during summer time in Massachusetts Bay. The generation, propagation and dissipation of these waves were simulated using FVCOM-NH. Building on the model's ability to successfully reproduce the major characteristics of internal waves observed in August 1998, we have examined the physical mechanism for the generation of internal waves over Stellwagen Bank. The mechanism-guided experiments suggest that the internal wave over the bank is generated in three distinct phases: (1) release of an initial density perturbation maintained on the crest of Stellwagen Bank during the previous ebb tide to form a large density front on the western side of the bank near ebb-flood transition; (2) nonlinear steepening of the density front into a deep density depres-

sion; and (3) evolution of the depression into a wave train owing to effects of dispersion and nonlinearity. Our results support the theory proposed by LB but not by *Maxworthy* [1979]. Our numerical experiments suggest that while a single massive density depression forms on the lee side during ebb tide, this mechanism does not contribute to the generation of high-frequency internal waves observed on the western side of Stellwagen Bank.

[39] Our case studies show that Earth's rotation should be taken in account in the study of high-frequency internal waves generated by Stellwagen Bank and in the interior of Massachusetts Bay. The Coriolis force tends to transfer the cross-bank tidal kinetic energy into the along-bank direction and thus reduces the intensity of the density front at ebb-flood transition and density depression in flood period. This process changes the geographic location of the wave's formation and also leads to faster propagation of the wave train.

[40] The inviscid assumption used in previous studies of internal waves in Massachusetts Bay is appropriate for mechanism-oriented studies but not for realistic simulation. Ignoring bottom friction significantly enlarges the cross-bank scale of the density front on the western flank of the bank near the ebb-flood transition and also causes an eastward shift of the front's location. The internal waves generated in this case feature a larger vertical density displacement and weaker dissipation when the waves shoal on the inner slope. Case studies with and without MY 2.5 turbulent parameterization of vertical mixing show little difference in the wave evolution processes. This suggests that vertical mixing may have marginal effect on internal waves in Massachusetts Bay.

[41] **Acknowledgments.** This research was supported by NOAA grants DOC/NOAA/NA04NMF4720332 and DOC/NOAA/NA05NMF4721131, U.S. GLOBEC Northwest Atlantic/Georges Bank Program NSF grants (OCE-0606928, OCE-0712903, OCE-0732084, OCE-0726851, OCE0814505), and MIT Sea Grant funds (2006-RC-103 and 2010-R/RC-116), NOAA NERACOOS Program for the UMASSD team and the Smith Chair in Coastal Oceanography, and NOAA grant (NA-17RJ1223) for R.C. Beardsley. C. Chen's contribution is also supported by Shanghai Ocean University under grants A-2302-10-0003 and 09320503700 and the State Key Laboratory for Estuarine and Coastal Research, East China Normal University. We would like to thank B. Butman for providing us the internal wave data observed during MBIWE98 and A. Scotti for helpful discussion during the model setup. The comments of two anonymous reviewers significantly helped us revise the original manuscript. We want to thank the FVCOM development team members in the Marine Ecosystem Dynamics and Modeling Laboratory, School of Marine Science and Technology, UMASSD, for their support and assistance in updating and improving the FVCOM code. We would also like to thank B. Rothschild for his continuous support in the development of FVCOM-NH. This paper is 10-1101 in the SMAST Contribution Series, School of Marine Science and Technology, University of Massachussetts Dartmouth, and U.S. GLOBEC contribution 687.

References

Armi, L., and D. M. Farmer (1988), The flow of Mediterranean water through the Strait of Gibraltar, *Prog. Oceanogr.*, *21*, 1–105, doi:10.1016/0079-6611(88)90055-9.

Baines, P. G. (1987), Upstream blocking and airflow over mountains, *Annu. Rev. Fluid Mech.*, *19*, 75–95, doi:10.1146/annurev.fl.19.010187.000451.

Balay, S., K. Buschelman, V. Eijkhout, W. Group, D. Kaushik, M. Knepley, L. G. McInnes, B. Smith, and H. Zhang (2007), *PETSc User Manual*, *Rep. ANL-95/11, Rev. 2.3.3*, 190 pp., Math. and Comput. Sci. Div., Argonne Natl. Lab., Argonne, Ill.

Butman, B., P. S. Alexander, A. Scotti, R. C. Beardsley, and S. Anderson (2006a), Large internal waves in Massachusetts Bay transport sediment offshore, *Cont. Shelf Res.*, *26*, 2029–2049, doi:10.1016/j.csr.2006.07.022.

Butman, B., P. S. Alexander, S. P. Anderson, F. L. Lightsom, A. Scotti, and R. C. Beardsley (2006b), *The Massachusetts Bay Internal Wave Experiment, August 1998: Data Report*, *Data Ser. 85* [DVD-ROM], U.S. Geol. Surv., Reston, Va. (Available at http://woodshole.er.usgs.gov/pubs/ds-85/WEBPAGES/title_page.html.)

Casulli, V. (1999), A semi-implicit finite-difference method for non-hydrostatic free-surface flows, *Int. J. Numer. Methods Fluids*, *30*, 425–440, doi:10.1002/(SICI)1097-0363(19990630)30:4<425::AID-FLD847>3.0.CO;2-D.

Chen, C., and R. C. Beardsley (1995), A numerical study of stratified tidal rectification over finite-amplitude banks, part I: Symmetric banks, *J. Phys. Oceanogr.*, *25*, 2090–2110, doi:10.1175/1520-0485(1995)025<2090:ANSOST>2.0.CO;2.

Chen, C., and R. C. Beardsley (1998), Tidal mixing over finite-amplitude banks: A model study with application to Georges Bank, *J. Mar. Res.*, *56*, 1163–1201, doi:10.1357/002224098765093607.

Chen, C., R. C. Beardsley, and R. Limeburner (1995), A numerical study of stratified tidal rectification over finite-amplitude banks, part II: Georges Bank, *J. Phys. Oceanogr.*, *25*, 2111–2128, doi:10.1175/1520-0485(1995)025<2111:ANSOST>2.0.CO;2.

Chen, C., H. Liu, and R. C. Beardsley (2003), An unstructured, finite-volume, three-dimensional, primitive equation ocean model: Application to coastal ocean and estuaries, *J. Atmos. Oceanic Technol.*, *20*, 159–186, doi:10.1175/1520-0426(2003)020<0159:AUGFVT>2.0.CO;2.

Chen, C., G. Cowles, and R. C. Beardsley (2006a), An unstructured grid, finite-volume coastal ocean model: FVCOM user manual, *Tech. Rep. 04-0601*, 183 pp., Sch. For Mar. Sci. and Technol., Univ. of Mass., Dartmouth, Mass.

Chen, C., R. C. Beardsley, and G. Cowles (2006b), An unstructured grid, finite-volume coastal ocean model (FVCOM) system, *Oceanography*, *19*, 78–89.

Chen, C., H. Huang, R. C. Beardsley, H. Liu, Q. Xu, and G. Cowles (2007), A finite-volume numerical approach for coastal ocean circulation studies: Comparisons with finite difference models, *J. Geophys. Res.*, *112*, C03018, doi:10.1029/2006JC003485.

Chereskin, T. K. (1983), Generation of internal waves in Massachusetts Bay, *J. Geophys. Res.*, *88*, 2649–2661, doi:10.1029/JC088iC04p02649.

Cowles, G. (2008), Parallelization of the FVCOM Coastal Ocean Model, *Int. J. High Perform. Comput. Appl.*, *22*, 177–193, doi:10.1177/1094342007083804.

Falgout, D. R., and U. M. Yang (2002), Hypre: A library of high performance preconditioners, in *Computational Science—ICCS 2007: 7th International Conference, Beijing China, May 27–30, 2007, Proceedings, Part III*, edited by P. M. A. Sloot et al., pp. 632–641, Springer, New York.

Farmer, D., and J. D. Smith (1978), Nonlinear internal waves in a fjord, in *Hydrodynamics of Estuaries and Fjords*, edited by J. Nihoul, pp. 465–514, Elsevier, New York.

Fringer, O. B., M. Gerritsen, and R. L. Street (2006), An unstructured-grid, finite-volume, nonhydrostatic, parallel coastal ocean simulator, *Ocean Modell.*, *14*, 139–173, doi:10.1016/j.ocemod.2006.03.006.

Gargett, A. E. (1976), Generation of internal waves in the Strait of Georgia, British Columbia, *Deep Sea Res.*, *23*, 17–32.

Gerkema, T. (1996), A unified model for the generation and fission of internal tides in a rotation ocean, *J. Mar. Res.*, *54*, 421–450, doi:10.1357/0022240963213574.

Halpern, D. (1971a), Semidiurnal tides in Massachusetts Bay, *J. Geophys. Res.*, *76*, 6573–6584, doi:10.1029/JC076i027p06573.

Halpern, D. (1971b), Observations on short-period internal waves in Massachusetts Bay, *J. Mar. Res.*, *29*, 116–132.

Haury, L. H., M. G. Briscoe, and M. H. Orr (1979), Tidally generated internal wave packets in Massachusetts Bay, *Nature*, *278*, 312–317, doi:10.1038/278312a0.

Helfrich, K. R., and W. K. Melville (2006), Long nonlinear internal waves, *Annu. Rev. Fluid Mech.*, *38*, 395–425, doi:10.1146/annurev.fluid.38.050304.092129.

Hibiya, T. (1988), The generation of internal waves by tidal flow over Stellwagen Bank, *J. Geophys. Res.*, *93*, 533–542, doi:10.1029/JC093iC01p00533.

Huang, H., C. Chen, G. W. Colwes, C. D. Winant, R. C. Beardsley, K. S. Hedstrom, and D. B. Haidvogel (2008), FVCOM validation experiments: Comparisons with ROMS for three idealized barotropic test problems, *J. Geophys. Res.*, *113*, C07042, doi:10.1029/2007JC004557.

Kanarska, Y., and V. Maderich (2003), A non-hydrostatic numerical model for calculating free-surface stratified flows, *Ocean Dyn.*, *53*, 176–185, doi:10.1007/s10236-003-0039-6.

Lai, Z., C. Chen, G. W. Cowles, and R. C. Beardsley (2010), A nonhydrostatic version of FVCOM: 1. Validation experiments, *J. Geophys. Res.*, *115*, C11010, doi:10.1029/2009JC005525.

Lee, C. Y., and R. C. Beardsley (1974), The generation of long nonlinear internal waves in weakly stratified shear flows, *J. Geophys. Res.*, *79*, 453–462, doi:10.1029/JC079i003p00453.

Loder, J. W. (1980), Topographic rectification of tidal currents on the sides of Georges Bank, *J. Phys. Oceanogr.*, *10*, 1399–1416, doi:10.1175/1520-0485(1980)010<1399:TROTCO>2.0.CO;2.

Mahadevan, A., J. Oliger, and R. Street (1996), A nonhydrostatic mesoscale ocean model. part II: Numerical implementation, *J. Phys. Oceanogr.*, *26*, 1881–1900, doi:10.1175/1520-0485(1996)026<1881:ANMOMP>2.0.CO;2.

Marshall, J., A. Adcroft, C. Hill, L. Perelman, and C. Heisey (1997), A finite-volume, incompressible Navier-Stokes model for studies of the ocean on parallel computers, *J. Geophys. Res.*, *102*, 5753–5766, doi:10.1029/96JC02775.

Maxworthy, T. (1979), A note on the internal solitary waves produced by tidal flow over a three-dimensional ridge, *J. Geophys. Res.*, *84*, 338–346, doi:10.1029/JC084iC01p00338.

Scotti, A., R. C. Beardsley, and B. Butman (2006), On the interpretation of energy and energy fluxes of nonlinear internal waves: An example from Massachusetts Bay, *J. Fluid Mech.*, *561*, 103–112, doi:10.1017/S0022112006000991.

Scotti, A., R. C. Beardsley, and B. Butman (2007), Generation and propagation of nonlinear internal waves in Massachusetts Bay, *J. Geophys. Res.*, *112*, C10001, doi:10.1029/2007JC004313.

Scotti, A., R. C. Beardsley, B. Butman, and J. Pineda (2008), Shoaling of nonlinear internal waves in Massachusetts Bay, *J. Geophys. Res.*, *113*, C08031, doi:10.1029/2008JC004726.

Trask, R. P., and M. G. Briscoe (1983), Detection of Massachusetts Bay internal waves by the synthetic aperture radar (SAR) on SEASAT, *J. Geophys. Res.*, *88*, 1789–1799, doi:10.1029/JC088iC03p01789.

Vlasenko, V., N. Stashchuk, and K. Hutter (2005), *Baroclinic Tides: Theoretical Modeling and Observational Evidence*, Cambridge Univ. Press, New York.

R. C. Beardsley, Department of Physical Oceanography, Woods Hole Oceanographic Institution, Woods Hole, MA 02543, USA.

C. Chen, G. W. Cowles and Z. Lai, School for Marine Science and Technology, University of Massachusetts Dartmouth, New Bedford, MA 02744, USA. (z.lai@umassd.edu)